International Journal of Plasticity 184 (2025) 104182

Contents lists available at ScienceDirect

International Journal of Plasticity

journal homepage: www.elsevier.com/locate/ijplas

Multiscale computational analysis of crack initiation at the grain boundaries in hydrogen-charged bi-crystalline alpha-iron

Yipeng Peng [a], Thanh Phan [b], Haibo Zhai [c,d], Liming Xiong [b,e], Xiang Zhang [a,*]

[a] Department of Mechanical Engineering, University of Wyoming, 1000 E. University Avenue, Laramie, 82071, WY, USA
[b] Department of Mechanical and Aerospace Engineering, NC State University, Raleigh, NC, 27695, USA
[c] Department of Civil & Architectural Engineering, University of Wyoming, 1000 E. University Avenue, Laramie, WY, 82071, USA
[d] Department of Engineering & Public Policy, Carnegie Mellon University, 5000 Forbes Avenue, Pittsburgh, PA, 15213, USA
[e] Department of Aerospace Engineering, Iowa State University, Ames, 50011, IA, USA

ARTICLE INFO

Keywords:
Hydrogen embrittlement
Grain boundaries
Cavitation
Crack initiation and growth
Dislocation
Diffusion
Atomistic-to-continuum simulations

ABSTRACT

This paper presents a mesoscale concurrent atomistic–continuum (CAC) simulation of crack initiation at the atomically structured grain boundaries (GBs) in bi-crystalline BCC iron (α-Fe) charged with hydrogen (H). By retaining the atomistic GB structure evolution together with the long-range dislocation-mediated plastic flow away from the GB in one model at a fraction of the cost of full molecular dynamics (MD), CAC enables us to probe the interplay between the atomic-level H diffusion, the nanoscale GB cavitation, crack initiation, growth, as well as the dislocation activities far away from the GB. Our several main findings are: (i) a tensile strain normal to the GB plane largely promotes the H diffusion towards the GB. (ii) the plasticity-induced clustering of H atoms (PICH) is identified as an intermediate process in between the H-enhanced localized plasticity (HELP) and H-enhanced de-cohesion (HEDE). (iii) PICH significantly amplifies the local stress concentration at the GB and decreases its cohesive strengths, and (iv) the GBs with different atomic structures fail differently. In detail, the H-charged $\Sigma 3$ GB fails through micro-twinning assisted void nucleation and coalescence, while the H-charged $\Sigma 9$ GB fails through crack initiation and growth accompanied by dislocation emission. Compared with nanoscale molecular dynamics (MD) simulations, the mesoscale CAC models get one step closer to the experimentally measurable length scales and thus predict reasonably lower GB cohesive strengths. This research addresses one key aspect of how H impacts the GB cohesive strengths in α-Fe. It offers insights into the multiscale processes of hydrogen embrittlement (HE). Our findings highlight the importance of using concurrent multiscale models, such as a combination of CAC, crystal plasticity finite element (CPFE), and cohesive zone finite element method (CZFEM), to understand HE. This will, in turn, support the development of new strategies for mitigating HE in a variety of engineering infrastructures.

1. Introduction

Hydrogen embrittlement (HE) constitutes a significant challenge in engineering, particularly affecting the durability and integrity of many infrastructures, such as oil pipelines, power plants, hydrogen vehicles, etc. This phenomenon occurs when hydrogen (H) atoms permeate the metallic lattice, which reduces ductility and often results in unexpected and catastrophic failure

* Corresponding author.
E-mail address: xiang.zhang@uwyo.edu (X. Zhang).

https://doi.org/10.1016/j.ijplas.2024.104182
Received 4 August 2024; Received in revised form 26 October 2024
Available online 23 November 2024

modes (Robertson et al., 2015; Martin et al., 2020). It has been aware and intensively studied since 1875 (Johnson, 1875) with various mechanisms being proposed.

The most representative two of them are: (i) The H-enhanced localized plasticity (HELP) (Ferreira et al., 1998; Kacher and Robertson, 2012; Birnbaum and Sofronis, 1994). HELP suggests that H promotes the mobility of dislocations, enhances a localized slip, and then a stress concentration for initiating a crack. (ii) By contrast, the H-enhanced de-cohesion (HEDE) (Pfeil, 1926; Lynch, 2011), argues that the presence of hydrogen in a metal can significantly weaken the bonds between metal atoms and leads to a reduced cohesive strength, which causes brittle fracture. Despite the great credibility of these two and many other similar mechanisms (Li et al., 2020; Isfandbod and Martínez-Pañeda, 2021; Fujihara et al., 2024; Wan et al., 2019; Liang et al., 2021; Song and Curtin, 2011, 2012; An et al., 2020), a commonly agreed wisdom that can address the full complexity of HE does not exist yet because: (a) These mechanisms often focus on only one aspect of HE by emphasizing the effects of H on material behavior at specific length scales, such as the effect of H on the mesoscale slip in HELP, or the H-induced atomic bond weakening in HEDE, instead of probing a synergy of several processes across multiple length scales. (b) These mechanisms either ignore the fine-scale structure changes induced by the atomic-level H diffusion (e.g., HELP) or ignore the far-field stresses induced by the collective dislocation (e.g., HEDE) or other defects activity away from the HE sites. As a consequence, not surprisingly, when the atomistic nature of H diffusion and dislocation core structure is considered, the dislocation mobility contradicts the prediction by HELP (Song and Curtin, 2014). Similarly, when the far-field stress is considered (Warner et al., 2007), dislocations do not always emit from the crack tip. but compete with twinning. Clearly, the mechanisms of H-induced damage are complex. It may be coupled with twinning (Khanchandani et al., 2023), phase transformations (Li et al., 2017), and void and crack nucleation in plastically deformed materials. A mechanistic understanding of it demands an in-depth analysis across a broad range of length scales.

From the experimental point of view, current efforts on HE studies at different scales rely on advanced techniques with different resolutions. For instance, to characterize the H-induced material microstructure change, high-resolution transmission electron microscopy (HRTEM) or high-resolution scanning electron microscopy (HRSEM) is often used to image the dislocation and GB configuration in an H-charged sample under deformation (Yin et al., 2019; Martin et al., 2019; Deng and Barnoush, 2018; Okuno and Takai, 2023; Robertson, 2001; Koyama et al., 2014; Kim and Tasan, 2019; Koyama et al., 2020; Gong et al., 2022; Huang et al., 2023). To characterize H diffusion dynamics and its dependence on the material microstructure, secondary ion mass spectrometry (SIMS) is often used for measuring the H concentration and distribution, offering a very high microstructure sensitivity and spatial resolution (Saintier et al., 2011). These experimental efforts aim to provide evidence to support the existing HE mechanisms. For instance, in HRTEM (Robertson, 2001), it was found that the spacing between dislocations in the pileup near a GB significantly decreases when the sample is charged with H. Such an observation was argued as one main evidence to support HELP by assuming that H has promoted the dislocation motion. Similarly, in SIMS (Saintier et al., 2011), it was found that H atoms tend to accumulate nearby dislocations, GBs, and voids, which can be considered as evidence for HEDE. Despite their great insights, these experimental results still need to be taken with caution because: (a) the sample preparation, such as the TEM sample preparation using the focused ion beam, may have introduced stress states largely deviating from that in bulk. (b) these experimental attempts focus on characterizing either the material microstructure, such as dislocation and GB configuration in HRTEM, or the H distribution, such as SIMS. Imaging of the simultaneous dislocation and GB structure evolution together with the H diffusion along the dislocations and GBs is not achieved until a recent attempt in Koyama et al. (2020). The hidden mechanisms underlying HE might have been missed from single-scale experiments. This thus necessitates high-fidelity simulations as a supplemental.

Historically, continuum mechanics-based computer simulations have enjoyed the most popularity in understanding HE by considering it a mechanical-diffusion coupling problem. As reviewed in Peng et al. (2023b), existing continuum models (Sofronis and McMeeking, 1989; Novak et al., 2010; Barrera et al., 2016; Zirkle et al., 2021; Asano and Otsuka, 1976; Beachem, 1972; Matsui et al., 1979; Ilin et al., 2014; Charles et al., 2017; Abdolvand, 2019; Arnaudov et al., 2020; Hassan et al., 2019; Hussein et al., 2021; Tondro et al., 2023; Li et al., 2023) can be used to characterize the homogenized behavior with the fine-scale hydrogen diffusion dynamics at the atomically structured GB being smeared out. To predict HE in polycrystalline materials, a two-way coupling model will be needed by being equipped with four necessary components: (a) an explicit model for the grain structure. (b) a crystal plasticity finite element (CPFE) solver to simulate how the material deforms with its constitutive models being decorated with the effect of H. (c) a diffusion equation to solve how the H concentration field evolves under the effect of local stresses. And (d) the H diffusivity and its dependence on local stresses and structures, such as pipe diffusion along the dislocations or GBs. Despite the importance of each component, it is always not so trivial to include all of them simultaneously. Existing models often only include a few among these four (Rimoli and Ortiz, 2010; Pu et al., 2017). Moreover, even though all four components are included, to achieve a high predictive capability, a two-way coupling model for polycrystalline samples with the grain structures retained still requires the constitutive rules to be carefully calibrated from either experiments or fine-scale, such as molecular dynamics (MD) simulations.

At the atomic scale, MD is one of the most popular simulation tools for studying H diffusion, dislocation motion, GB cavitation, cracking, and their interaction with each other. By tracking the motion of each atom, extensive MD simulations were performed to show: (1) H diffusion around a screw dislocation core is much slower than that away from the core (Kimizuka and Ogata, 2011). (2) the H diffusion energy barrier exhibits an obvious dependence on the structures of dislocation cores, GBs, and triple junctions (Sanchez et al., 2010; Zhou et al., 2021). (3) the H aggregation at the crack tip suppresses the dislocation emission and causes a ductile-to-brittle transition in BCC iron (Song and Curtin, 2012). (4) the critical 'pop-in' forces in the nanoindentation tests on an H-charged sample are significantly lower than that without H (Zhou et al., 2016b; Yavas et al., 2020), and among many others (Song and Curtin, 2014; Chen et al., 2021). Although MD simulations have largely advanced our understanding of HE, a direct usage of the results from such simulations to explain the experimental results was often taken with conservation for two reasons. Firstly, due to its high computational cost, the simulation cell in MD is usually limited to tens of nanometers. Consequently, the

dislocation density and H concentration in MD are often unrealistically high. Secondly, the long-range stress induced by accumulating a large population of dislocations at the GBs (Guo et al., 2015) spans a range of micrometers and is often cut off in MD.

Clearly, neither continuum nor atomistic models alone can cover the full spectrum of the complexity of HE, which involves the interaction between H diffusion, dislocation plasticity, GB cavitation, and cracking. A multiscale model that can take advantage of both continuum and atomistic models but can overcome their limitations is needed. This model should: (i) scale up in length to accommodate the mesoscale dislocation activities and grain structures but retain the atomistic resolution for dislocation core, GBs, and H diffusion. (ii) Abandon the deployment of empirical constitutive rules, which assume fast/slow H diffusion along the material defects and H-induced softening/hardening, by using the interatomic force field as the only input but requiring a significantly less computational cost than that by MD. (iii) Allow H diffusion, dislocation migration, and crack propagation in both atomistic and continuum domains without the need for any additional treatments.

We argue that a recent concurrent atomistic–continuum (CAC) method developed by Xiong and co-workers (Xiong et al., 2012b; Xu et al., 2018, 2017; Chen et al., 2018; Ji et al., 2024; Xiong and Chen, 2009b; Ji et al., 2022) satisfies these needs and will be thus deployed here. CAC was shown to be capable of modeling: (1) the long-range internal stress concentration induced by the reaction between a microscale slip containing a large population of dislocations and an atomically structured GB (Peng et al., 2022). (2) the relaxation of such a stress concentration by H diffusion (Peng et al., 2023b), dislocation transmission (Su et al., 2023), twinning and phase transformation (Peng et al., 2023a) across the GB.

For the first time in this work, CAC simulations accommodate the atomic-level H diffusion, nanoscale GB cavitation, and cracking, as well as the mesoscale dislocation slip away from the atomically structured GB all in one model. Compared with existing models for simulating HE, CAC brings benefits in two main aspects. Firstly, it is a two-way deformation–diffusion coupled model without smearing out the atomistic nature of H diffusion, dislocation emission, and GB crack initiation. Secondly, it requires the interatomic potential as the only constitutive input but expands the predictive capability of MD simulations from the nanoscale to the mesoscale at a fraction of the cost of MD. As a consequence of these two benefits, the CAC simulation tool will offer us an alternative vehicle that can be used to arrive at a mechanistic understanding of HE by characterizing its multiscale nature at an unprecedented fidelity. In this study, taking the bi-crystalline alpha-iron containing a typical tilt GB as an example, the coupled dynamics between H diffusion, GB cavitation, cracking, dislocation emission, and migration away from the GB will be characterized by CAC. In the rest of this paper, we will first introduce the methodology and model set-up in Section 2. The simulation results will be analyzed and discussed in Section 3. We will then end this paper with a summary of our major findings in Section 4 and then a brief discussion of future attempts in Section 5.

2. Methodology and computational model setup

The CAC model for a sub-micron-sized bi-crystalline BCC iron sample (dimension: 356 nm × 672 nm × 7 nm) containing a tilt GB charged with H is illustrated in Fig. 1. The CAC simulation tool is built upon the finite element (FE) implementation of a formulation (Chen, 2006, 2009; Chen and Diaz, 2016; Chen, 2016; Chen and Diaz, 2018; Chen, 2024) that unifies the atomistic and continuum description of materials via Kirkwood's statistical mechanical theory of transport processes (Kirkwood, 1946, 1947; Irving and Kirkwood, 1950; Bearman and Kirkwood, 1958). In this formulation, continuum quantities, such as mass, energy, and stress, are defined in terms of atomistic forces, displacement, and velocities, respectively. Atomistic-informed balance equations were then derived, which are analogous to the balance equations in continuum mechanics but with atomistic information built in. Thus, continuum modeling techniques, such as FE, can be used to solve them. The discretization of a sample, such as the interior of Grain-I and Grain-II in Fig. 1a, into these FEs leads to a coarse-grained (CG) description of materials (Chen et al., 2018; Ji et al., 2024, 2022; Xiong and Chen, 2009a; Xiong et al., 2011, 2012a,c). Such a CG description of materials by FE has three unique features: (1) Each FE in the CG domain is a collection of crystal lattice cells. (2) The forces acting on the Gauss quadrature points and then the FE nodes are derived and calculated (Xiong et al., 2011) from the interatomic force fields, such as the Embedded Atom Method (EAM) force field for Iron (Fe)-Fe and Fe-H (H) interactions (Song and Curtin, 2012) used in this work. (2) The FE in the CG domain is carefully designed, with the boundaries between FEs being aligned along the slip planes of the materials under consideration. This alignment ensures that post-nucleation, both smooth (Chen et al., 2018; Xiong et al., 2011, 2012a,c) and rough dislocations (Ji et al., 2024, 2022) can migrate along the FE boundaries. Without the need for any special numerical treatments, this model can seamlessly transfer dislocations and also cracks (Xiong et al., 2012b; Peng et al., 2022, 2023a; Yang and Chen, 2015) between atomistic and FE domains in a self-consistent manner. In this way, CAC provides us with a unique platform to simulate the atomistic-to-nanoscale cavitation, crack nucleation, and growth of an H-charged GB, as well as the mesoscale dislocation activities in a far field away from the GB.

As a demonstration of the unique capability of CAC, two particular GBs, $\Sigma 3$ and $\Sigma 9$ symmetric tilt grain boundaries (STGBs), are selected and considered here. Instead of simulating the long-term slow H segregation from the far field into the GB, here, 79,000 H atoms are directly inserted into the atomistic domain near the GB. The Fe-Fe and Fe-H interactions are described using the EAM force field (Song and Curtin, 2012). This approximately leads to an H concentration of 0.074 mol/L for the sample dimension under consideration here. The initial positions of those H atoms are random, and their distribution is initially uniform in space. To the best of our knowledge, two strategies are mostly commonly used in the literature to achieve a relatively realistic H distribution on the GBs: (i) one is to introduce hydrogen into certain favorable sites on the GB, which were identified through density functional theory calculations, such as the work (Zhou et al., 2016a). (ii) the other is to use a combined kinetic Monte Carlo and MD to generate many sets of initial models and then choose the one with lower potential energy, such as that in Barrows et al. (2016). In this paper, we introduce H atoms into GB randomly and then relax the H-charged GB. It is not as rigorous as the two approaches above but is

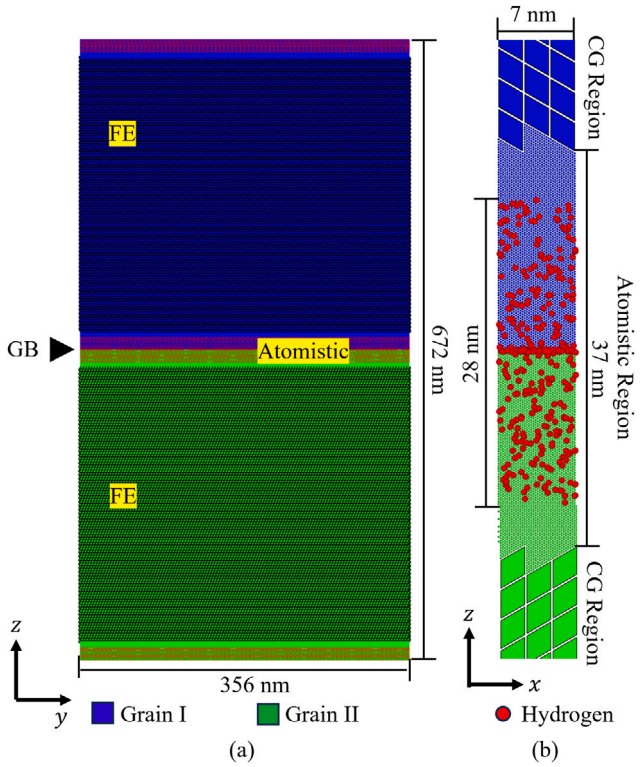

Fig. 1. The mesoscale CAC computer model set-up for a bi-crystalline BCC iron containing a tilt GB charged with H: (a) coarse-grained (CG) description of Grain I (blue) and Grain II (green) by finite element (FE) together with the atomistic description of the GB charged with H within one model. The dimensions of the grains are annotated; (b) Zoom-in view of the GB domain in the model highlighting the atomistic resolution near the GB and the FE configuration in the CG region away from the atomically structured GB. (For interpretation of the references to color in this figure legend, the reader is referred to the web version of this article.)

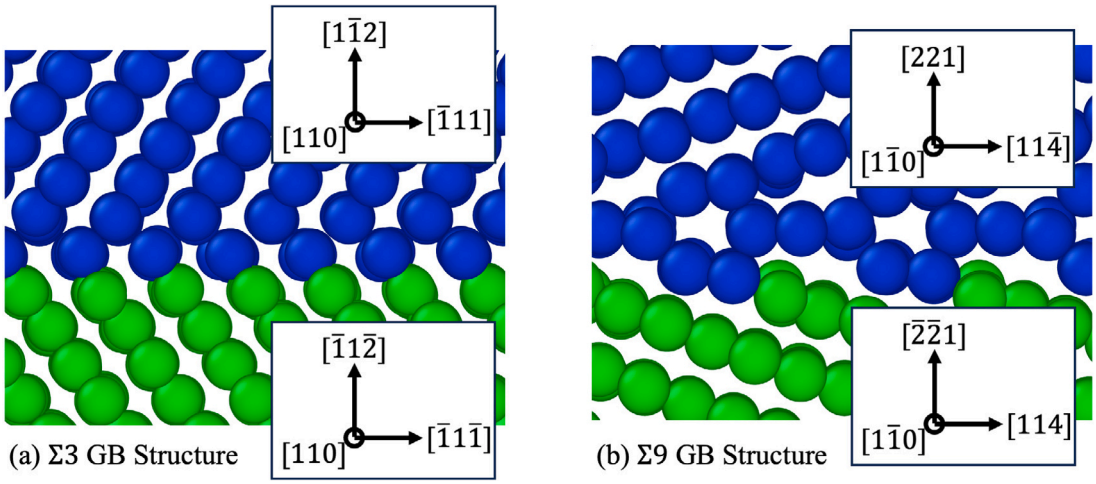

Fig. 2. The atomic configurations at (a) $\Sigma 3$ and (b) $\Sigma 9$ GBs, respectively, with atoms in Grain I being colored with blue and that in Grain II with green. (For interpretation of the references to color in this figure legend, the reader is referred to the web version of this article.)

close to that in Barrows et al. (2016). We have performed several sets of additional simulations with different initial H distributions and found that the simulation results remain qualitatively the same as what has been reported here.

The configuration with very small Fe-H and H-H separations will be avoided, as shown in Fig. 1b. For $\Sigma 3$ GB, the lattice orientations are chosen to be $x[110]$, $y[\bar{1}11]$, and $z[1\bar{1}2]$ in Grain-I; and $x[110]$, $y[\bar{1}\bar{1}\bar{1}]$, and $z[\bar{1}\bar{1}2]$ in Grain-II (see Fig. 2a), respectively. For $\Sigma 9$ GB, the lattice orientations are chosen to be $x[1\bar{1}0]$, $y[11\bar{4}]$, and $z[221]$ in Grain-I; and $x[1\bar{1}0]$, $y[114]$, and $z[\bar{2}\bar{2}1]$ in Grain-II

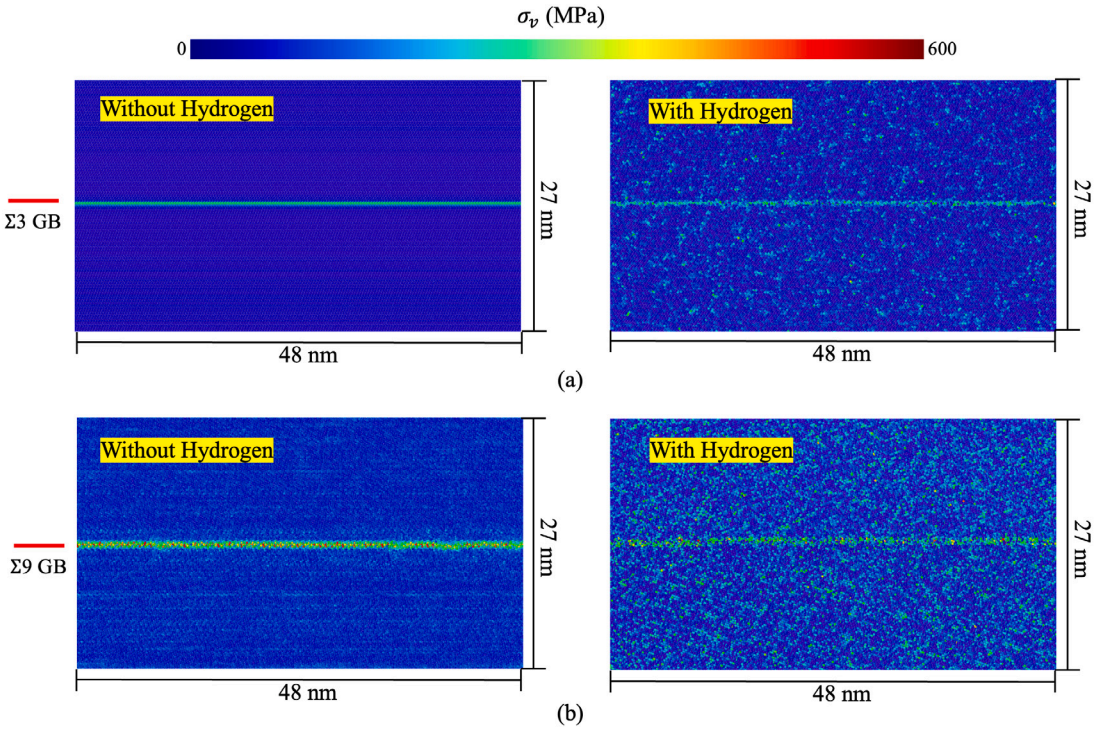

Fig. 3. The local Von-Mises stress σ_v near (a) $\Sigma 3$ and (b) $\Sigma 9$ GBs calculated with Eq. (1) in the absence and presence of H, respectively.

(see Fig. 2b), respectively. Each FE in the CG region away from the GB contains 1728 atoms. The model encompasses roughly 77,000 FEs and ≈17.4 million discrete atoms at the GBs. If one relies on full MD to model this system, it will contain 150 million atoms. Thus, deployment of CAC here leads to a gain of computational efficiency by reducing the number of degrees of freedom to 12% of a full MD model. The thickness of the atomically structured GB region is 37 nm (see Fig. 1b). To simulate the GB cavitation, crack initiation, and growth under the effect of H diffusion, the bi-crystalline model is then deformed under a uniform stretch along a direction perpendicular to the GB plane. A constant temperature (Ji et al., 2024, 2022) of 300 K is imposed. The equation of motion is integrated with a time step of 0.001 ps. Periodic boundary conditions (PBCs) are applied along all three directions of the model.

It should be noted that the geometric setup deployed in our simulations also acknowledges the tri-axial nature of void nucleation, GB crack initiation, and growth. Although a three-dimensional setup is often desired to support the interpretation of the experimental observations, here we use a thin-layer model with PBCs along the x-direction as an approximation to plane strain for reducing the computational cost. This setup is reasonably appropriate for symmetric tilt GBs, where the effects outside the yz-plane are less significant. We have also conducted a sensitivity analysis to demonstrate that the thin-layer approximation does not significantly alter the results for these specific GB configurations. Also, we adopted a stress-controlled loading strategy to deform the sample here. In detail, the tensile stress applied on the sample is gradually increased at each time step and then the system was equilibrated after each time step to ensure that the stress–strain curves represent the material's constitutive response to a quasi-static loading.

3. Simulation results

3.1. GB stresses, free volumes, and H diffusion at the GBs

With an atomistic resolution at the GB, CAC enables us to calculate the local stresses, free volumes, and H diffusion coefficient, all at atomic scales. Given the dynamic nature of the present CAC run, it should be pointed out that the atomic stresses and volumes presented here are from a time averaging of them in a duration of 20 ps.

The local stresses from CAC simulations of the relaxation of the bi-crystalline BCC iron containing $\Sigma 3$ (Fig. 3a) and $\Sigma 9$ GBs (Fig. 3b) in the absence/presence of H are analyzed here. For simplicity, a Virial stress formula (Chen, 2016), rather than the recent mechanical stress (Chen, 2016; Ji et al., 2018), was used here for calculating the six stress components on each atom, although the mechanical stress was shown to be unconditionally consistent while the Virial stress formula was conditionally consistent with the concept of Cauchy stress in continuum mechanics (Chen, 2016) . The Von Mises stress noted as σ_v, is then calculated from the six stress components through:

$$\sigma_v = \left\{ \frac{1}{2}[(\sigma_{xx} - \sigma_{yy})^2 + (\sigma_{yy} - \sigma_{zz})^2 + (\sigma_{zz} - \sigma_{xx})^2] + 3(\tau_{xy}^2 + \tau_{yz}^2 + \tau_{zx}^2) \right\}^{\frac{1}{2}} \quad (1)$$

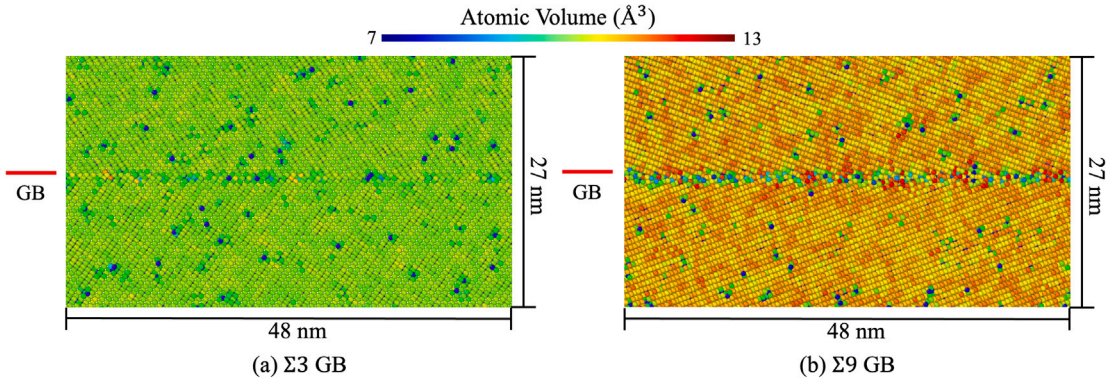

Fig. 4. The atomic volume analysis near (a) $\Sigma 3$ and (b) $\Sigma 9$ GBs in the absence and presence of H, respectively.

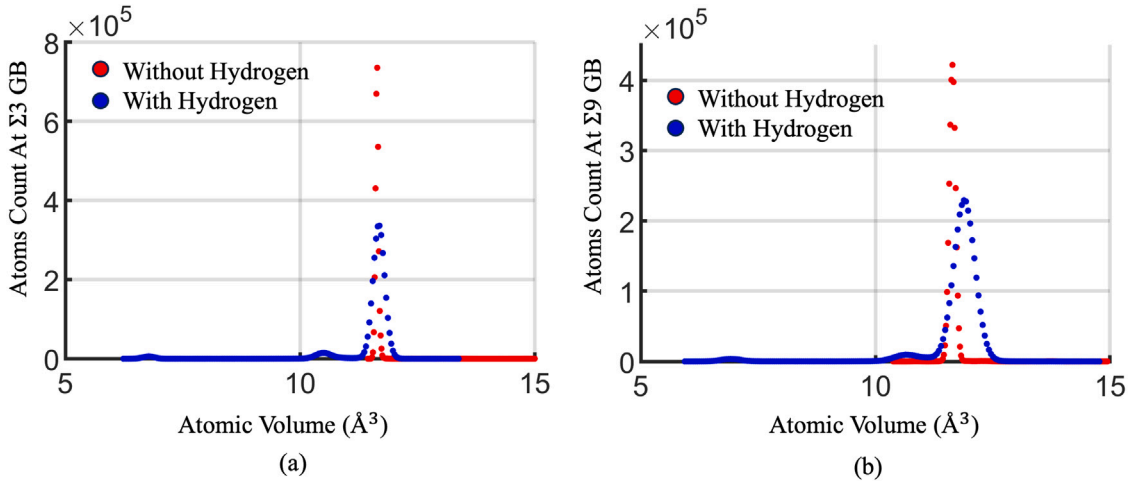

Fig. 5. The atomic volume analysis near the (a) $\Sigma 3$ and (b) $\Sigma 9$ GBs in the presence of H, respectively. (For interpretation of the references to color in this figure legend, the reader is referred to the web version of this article.)

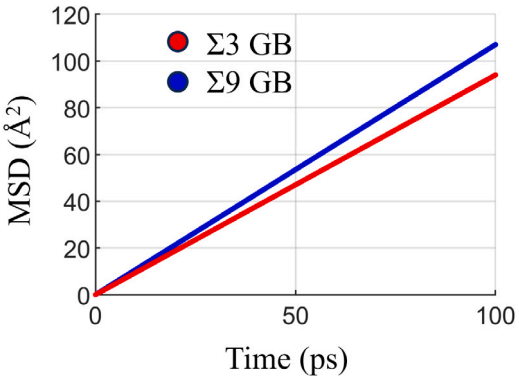

Fig. 6. The MSD curves resulting from CAC simulations of H atom diffusion at $\Sigma 3$ and $\Sigma 9$ GBs. (For interpretation of the references to color in this figure legend, the reader is referred to the web version of this article.)

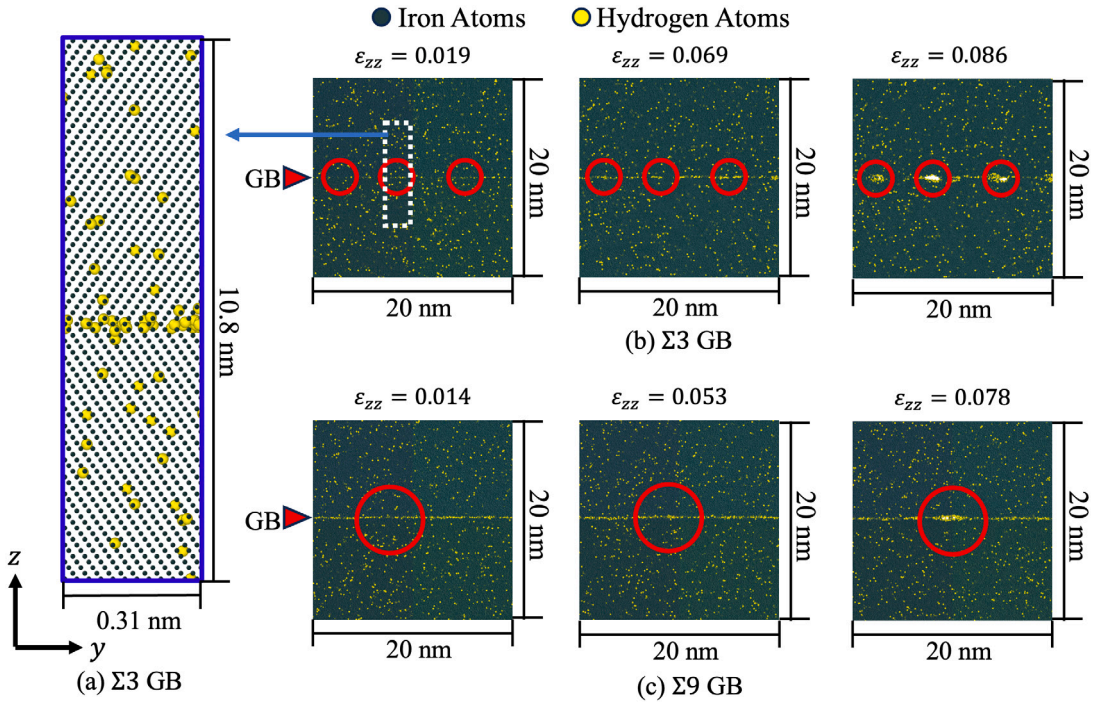

Fig. 7. (a) Initial grain boundary structure with hydrogen, and strain sequences of the snapshots of the H (yellow) clustering process near (b) $\Sigma 3$ and (c) $\Sigma 9$ GBs, respectively, with potential void and crack initiation sites being circled in red. (For interpretation of the references to color in this figure legend, the reader is referred to the web version of this article.)

Several major observations from Von Mises distribution in Fig. 3 are: (a) The residual stresses at the GB after the relaxation are considerably higher than those away from the GB. (b) The residual stresses at the $\Sigma 9$ GB are higher and span a longer range than that near the $\Sigma 3$ GB. (c) An insertion of H into the model enhances the stress heterogeneity near the GBs, and (d) the H-charged $\Sigma 9$ exhibits a stronger stress heterogeneity than $\Sigma 3$ GB does.

As a conjugate to local stress analysis, to quantify the H-induced structural changes, the time-averaged atomic volume analysis is also performed here. Relevant results are presented in Figs. 4 and 5. For the instantaneous atomic configuration at each time step, the atomic volume associated with each atom on the GB was calculated through two steps. Firstly, a Wigner–Seitz cell (Wigner and Seitz, 1933) around each atom on the GB is constructed. Then, the volume of each Wigner–Seitz cell is calculated and assigned as the volume of the atom under consideration.

Fig. 4 shows the atomic volume distribution near the H-charged $\Sigma 3$ and $\Sigma 9$ GBs, respectively, with a time-averaging of the instantaneous atomic configuration over a duration of 20 ps. It is observed that, for the $\Sigma 9$ GB, after charging it with H, the volumes around a majority of atoms are 12 $Å^3$, whereas they are only 11 $Å^3$ at the $\Sigma 3$ GB. To confirm it, Fig. 5 shows the statistical analysis of the atomic volumes near the H-charged $\Sigma 3$ and $\Sigma 9$ GBs, respectively. The horizontal axis of Fig. 5 is the atomic volume, and the vertical axis of it is the population of the atoms carrying that volume. Here, the volumes of each atom in a thin domain with a thickness of ≈30 nm around the GB are calculated and then condensed into the histogram in Fig. 5.

Several main findings from Fig. 5 are: (1) Peaks appear in the histograms for both $\Sigma 3$ and $\Sigma 9$ GBs, but the atomic volumes nearby $\Sigma 9$ GB span a wider range than that nearby the $\Sigma 3$ GB. The reason is that, for $\Sigma 3$ GB, the atoms near the GBs are densely packed in the same manner as they are within the domain away from the GB. As a consequence, the peak in Fig. 5a for $\Sigma 3$ GB occurs at 10 $Å^3$, which is the volume around an atom in a perfect BCC iron. Instead, for $\Sigma 9$ GB, due to the presence of the open atomic structures, which largely deviate from the dense atomic packing in BCC iron, a broad peak appears in Fig. 5b. (2) When the sample is charged with H, in both $\Sigma 3$ and $\Sigma 9$ GBs, the peaks in the histograms shift from smaller atomic volumes to a large end (or from left to right in Fig. 5b). Such peaks shift more (from 10 $Å^3$ to 11 $Å^3$) in $\Sigma 9$ GB than they do (from 10 $Å^3$ to 10.5 $Å^3$) in $\Sigma 3$ GB. This observation implies that charging the sample with H introduces more free volumes at $\Sigma 9$ GB than it does at $\Sigma 3$ GB. (3) In addition to the shift of a peak, charging the sample with H has also caused a broadening of the peaks. The H-induced peak broadening in $\Sigma 9$ GB is more substantial, highlighting a greater variation in atomic volumes than that in $\Sigma 3$ GB. It is thus believed that the presence of H causes more structure changes in the GB with open structures, such as $\Sigma 9$, than that in a dense GB, such as $\Sigma 3$.

As a consequence of such a difference in H-induced structure changes, the H diffusion dynamics at $\Sigma 9$ GB differs from that at $\Sigma 3$ GB. To characterize the local diffusivity near the GB, after the whole system was equilibrated for 20ps, we calculate the

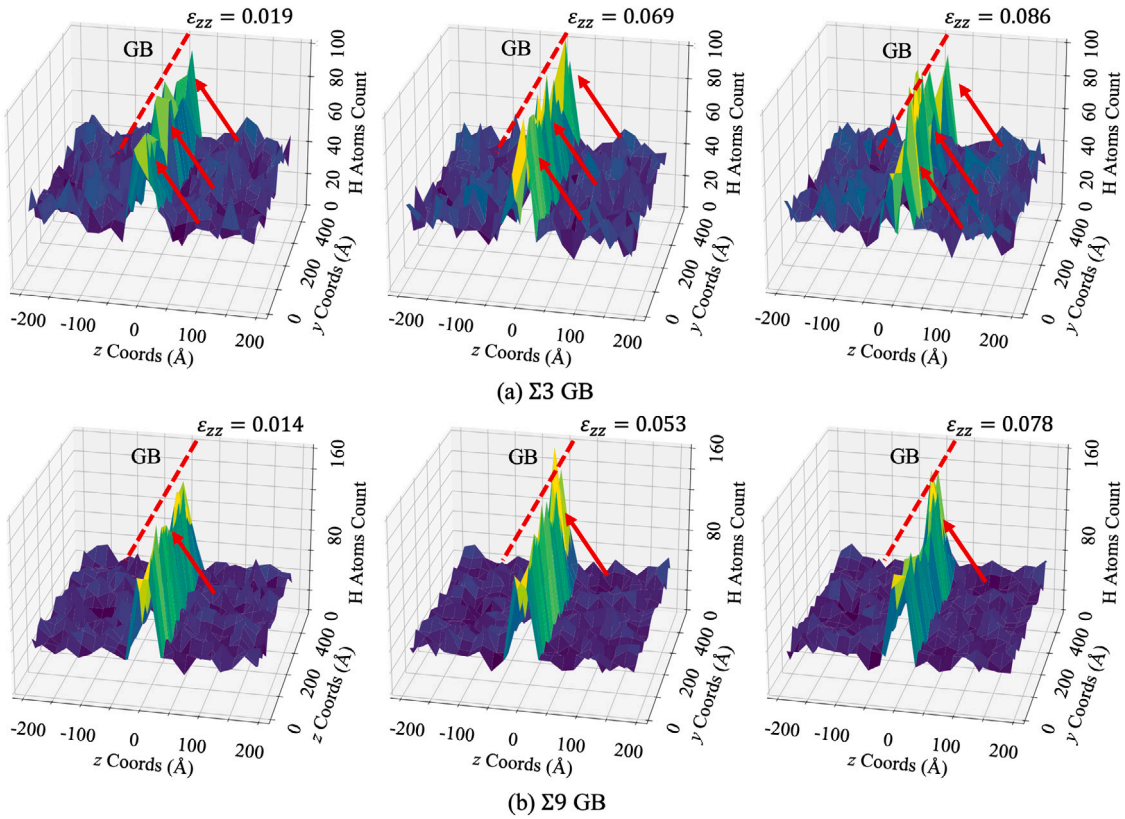

Fig. 8. Strain sequences of the snapshots of the hydrogen concentration profile near (a) $\Sigma 3$ and (b) $\Sigma 9$ GBs, respectively. Color from blue to yellow indicates the relative value from low to high. Voids and cracks are pointed with red arrows. (For interpretation of the references to color in this figure legend, the reader is referred to the web version of this article.)

mean square displacement (MSD) of H atoms over a duration of 100 ps. A calculation of the MSD provides us with opportunities to calculate the local H diffusion coefficient, D, as a first derivative of the MSD curve with respect to time. This will lead to a quantitative description of the collective motion of the H atoms on the GB. The diffusion coefficient is a critical factor in HE because it quantitatively reflects the propensity of the H atom's migration through the materials, especially the GBs, a process that may culminate in material degradation.

In this work, MSD is calculated using the equation as below:

$$\mathrm{MSD} = \lim_{t\to\infty} \frac{1}{6N} \sum_{i=1}^{N} \langle |\mathbf{x}(t) - \mathbf{x}(0)|^2 \rangle = \frac{1}{6} \lim_{t\to\infty} \frac{1}{N} \sum_{i=1}^{N} |\mathbf{x}^{(i)}(t) - \mathbf{x}^{(i)}(0)|^2 \tag{2}$$

where N represents the number of H atoms considered in the calculation, and $\mathbf{x}(t)$ denotes the position vector of the ith H atom at time t, relative to its initial position $\mathbf{x}(0)$. Fig. 6b shows the CAC simulation-predicted MSD curves for H diffusion along $\Sigma 3$ (red) and $\Sigma 9$ GBs (blue), respectively. Obviously, the slope of the red curve for $\Sigma 3$ GB is smaller than that for $\Sigma 9$ GB. It suggests that the H atom diffuses more slowly at $\Sigma 3$ GB than it does at $\Sigma 9$ GB. This corresponds well to the previous local stress and atomic volume analysis results because an easier H diffusion will be expected at the $\Sigma 9$ GB, where higher local stress and larger atomic volumes are present. Quantitatively, the H diffusion coefficient near the $\Sigma 3$ GB is 9.4×10^{-9} m^2/s and $1.07 \times 10^{-}8$ m^2/s at the $\Sigma 9$ GB, respectively. This is consistent with that from recent MD simulations and experimental study (Strauch et al., 2023).

3.2. H clustering, dislocation emission, cavitation, and cracking at the GBs

After relaxation, the simulation cell is deformed under tension along a direction normal to the GB plane. The deformation is realized through a stress-controlled loading strategy. In detail, tension was imposed by elongating the simulation cell until a desired stress along the z direction was achieved.

Fig. 7 presents the strain sequences of snapshots of the H diffusion process near $\Sigma 3$ and $\Sigma 9$ GBs under tension. In this figure, iron atoms are illustrated in blue, and H atoms are shown in yellow. The red circles highlight the regions where H atom clusters start to form. The snapshots are taken starting from the onset of plastic deformation until the onset of GB de-cohesion. Fig. 7 provides a clear view of the diffusion dynamics of H atoms at different tensile strains. Initially, at a lower level of strain (ε_{zz} = 0.019 for

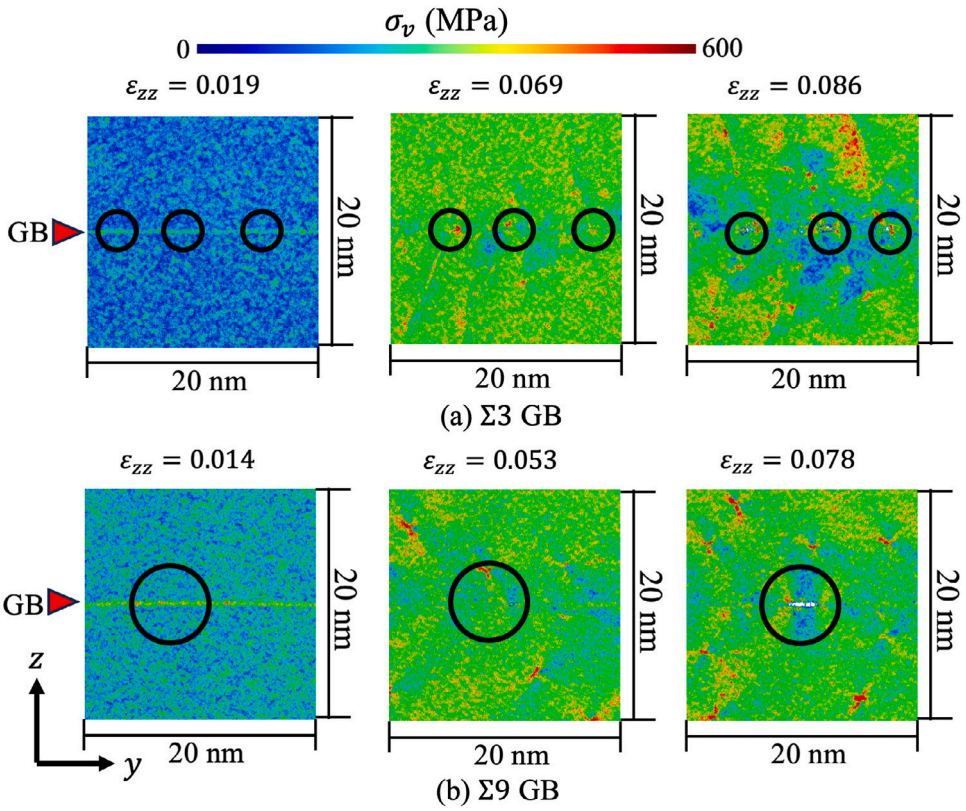

Fig. 9. Strain sequences of the snapshots of the von Mises stress distribution near (a) Σ3 and (b) Σ9 GBs, respectively, with potential void/crack initiation sites circled in black. (For interpretation of the references to color in this figure legend, the reader is referred to the web version of this article.)

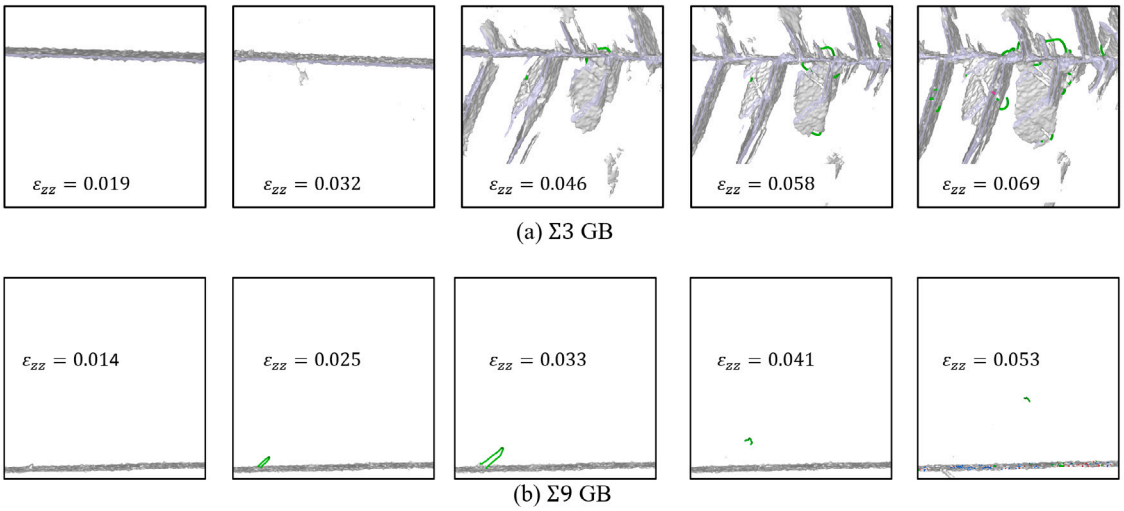

Fig. 10. Strain sequences of the snapshots showing the defect structure evolution near (a) Σ3 and (b) Σ9 GBs under a tension normal to the GB plane. OVITO (Stukowski, 2009) has been used here to show the defects around the GB. Dislocations are displayed in green. GB and stacking faults are shown in gray. (For interpretation of the references to color in this figure legend, the reader is referred to the web version of this article.)

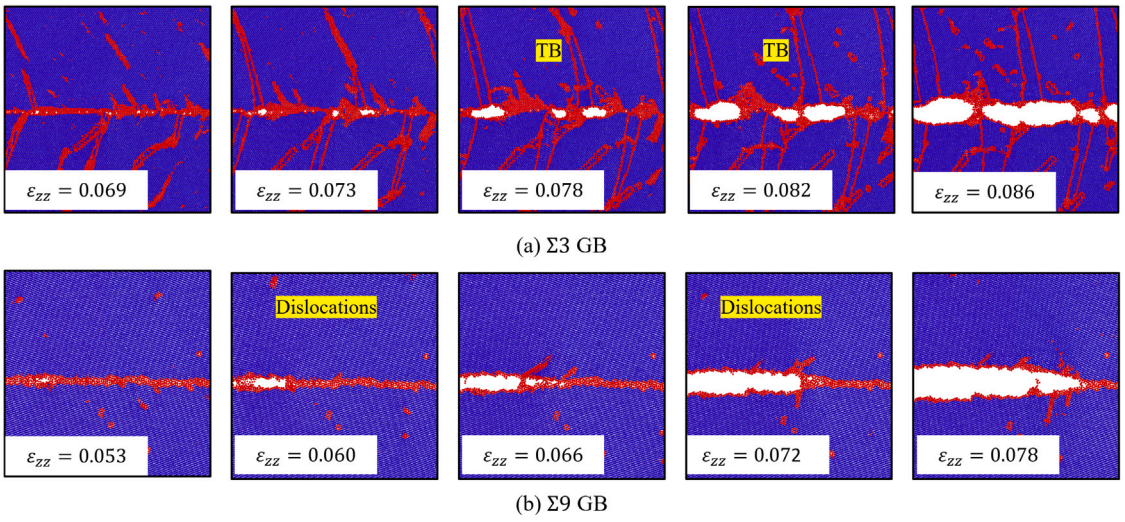

Fig. 11. Strain sequences of snapshots showing the defect structure evolution and subsequent failure (cavitation and cracking) process for: (a) $\Sigma 3$, and (b) $\Sigma 9$ GBs, respectively. Only the iron atoms near the GBs are displayed here. The atoms are colored according to their centrosymmetry parameters in OVITO (Stukowski, 2009). The blue color indicates a perfect atomic configuration in BCC iron, and the red color indicates the defects deviating from the BCC atomic configurations. (For interpretation of the references to color in this figure legend, the reader is referred to the web version of this article.)

$\Sigma 3$ GB and $\varepsilon_{zz} = 0.014$ for $\Sigma 9$ GB), H atoms intend to migrate towards the GBs, indicating the early stages of hydrogen clustering. When the applied strain increases, the H clusters form, especially visible in the middle and right images for both $\Sigma 3$ and $\Sigma 9$ GBs. The red circles indicate the sites where the significant accumulation of H atoms appears. For the $\Sigma 3$ GB, this phenomenon becomes evident at a strain of $\varepsilon_{zz} = 0.069$. By contrast, for $\Sigma 9$ GB, such H atom clustering is observed at a slightly lower strain of $\varepsilon_{zz} = 0.053$. These H clustering spots act as preferential sites for void nucleation and will contribute to material failure eventually. Upon a continuous increase of the strain ($\varepsilon_{zz} = 0.069$ and $\varepsilon_{zz} = 0.086$ for $\Sigma 3$ GB; $\varepsilon_{zz} = 0.053$ and $\varepsilon_{zz} = 0.078$ for $\Sigma 9$ GB), such a plastic deformation-induced clustering of H atoms (PICH) at the GBs further intensifies.

To quantitatively correlate the H concentration profile with the deformation, as a post-processing procedure, the samples near the GBs are divided into several finite-sized columnar-shaped volumes (7 nm × 2 nm × 2 nm). The axis of each columnar volume is along the sample thickness direction (x direction in Fig. 1). At each frame of the CAC simulation results, the number of H atoms within each columnar volume is counted. Fig. 8 shows the H atom concentration profile near the $\Sigma 3$ and $\Sigma 9$ GBs under different tensile strain. The top row in Fig. 8a presents the H concentration profile nearby the $\Sigma 3$ GB when the applied strain is $\varepsilon_{zz} = 0.019$, $\varepsilon_{zz} = 0.069$, and $\varepsilon_{zz} = 0.086$. The bottom row in Fig. 8b presents the H concentration profile nearby the $\Sigma 9$ GB when the applied strain is $\varepsilon_{zz} = 0.014$, $\varepsilon_{zz} = 0.053$, and $\varepsilon_{zz} = 0.078$, respectively. The y and z coordinates in Fig. 8 represent the positions of the center of each columnar volume, and the vertical axis in Fig. 8 is for the number of H atoms in that columnar volume under consideration.

Our several main observations from Fig. 8 are: (a) For both models, at all different strain levels, the H concentration at the GB is significantly higher than that away from the GB. (b) Upon an increase of the tensile strain, the H-concentration profile gradually narrows down to the GB domain in both $\Sigma 3$ (Fig. 8a) and $\Sigma 9$ (Fig. 8b) models. It means that the applied tensile strain promotes the H diffusion and segregation towards the GB. (c) Multiple H concentration peaks appear at the $\Sigma 3$ GB when $\varepsilon_{zz} = 0.086$ (Fig. 8a). And (d) by contrast, only one main peak of the H concentration is seen at the $\Sigma 9$ GB when $\varepsilon_{zz} = 0.078$ (Fig. 8b). Such different H concentration profiles at $\Sigma 3$ and $\Sigma 9$ GBs are believed to be responsible for the subsequent different failure mechanisms to be detailed next. That is, for $\Sigma 3$ GB, several nano-voids simultaneously nucleate at multiple H concentration sites. For the $\Sigma 9$ model, a main crack nucleates at the site where the H concentrates the most and then grows along the GB.

In parallel to the H concentration profile, Fig. 9 illustrates the Von Mises stress (σ_v) distribution near the $\Sigma 3$ GB (Fig. 9a) and $\Sigma 9$ GBs (Fig. 9b) under different tensile strain. The atoms are color-coded with their Von Mises stress values. The blue color represents a low-stress level, while the red color represents a high-stress level.

At the early stage of the deformation ($\varepsilon_{zz} = 0.019$ for $\Sigma 3$ GB and $\varepsilon_{zz} = 0.014$ for $\Sigma 9$ GB), the stress distribution is relatively uniform with a minor concentration at the GBs. When ε_{zz} continuously increases, stress concentrations start to develop at the GBs. For the $\Sigma 3$ GB, this becomes evident at $\varepsilon_{zz} = 0.069$ and intensifies at $\varepsilon_{zz} = 0.086$. For the $\Sigma 9$ GB, such a stress concentration begins at $\varepsilon_{zz} = 0.053$ and further intensifies at $\varepsilon_{zz} = 0.078$. A comparison of Fig. 9 and Fig. 8 shows that these stress concentration sites correspond well to the previously identified H clustering sites.

Accompanied by the plasticity-induced clustering of hydrogen and stress localization at the GB, defects start to appear near the GB. Fig. 10 shows the strain sequences of the snapshots of the defect structure evolution. A fully atomistic resolution at the GB, together with the positions of the atoms being interpolated from the FE nodal positions away from the GB, enables us to employ the dislocation analysis algorithm (DXA) in OVITO (Stukowski, 2009; Stukowski et al., 2012) to extract the local dislocation and stacking fault structure evolution. Fig. 10 shows that: (a) for $\Sigma 3$ GB, when the tensile strain ε_{zz} reaches 0.032, stacking faults start

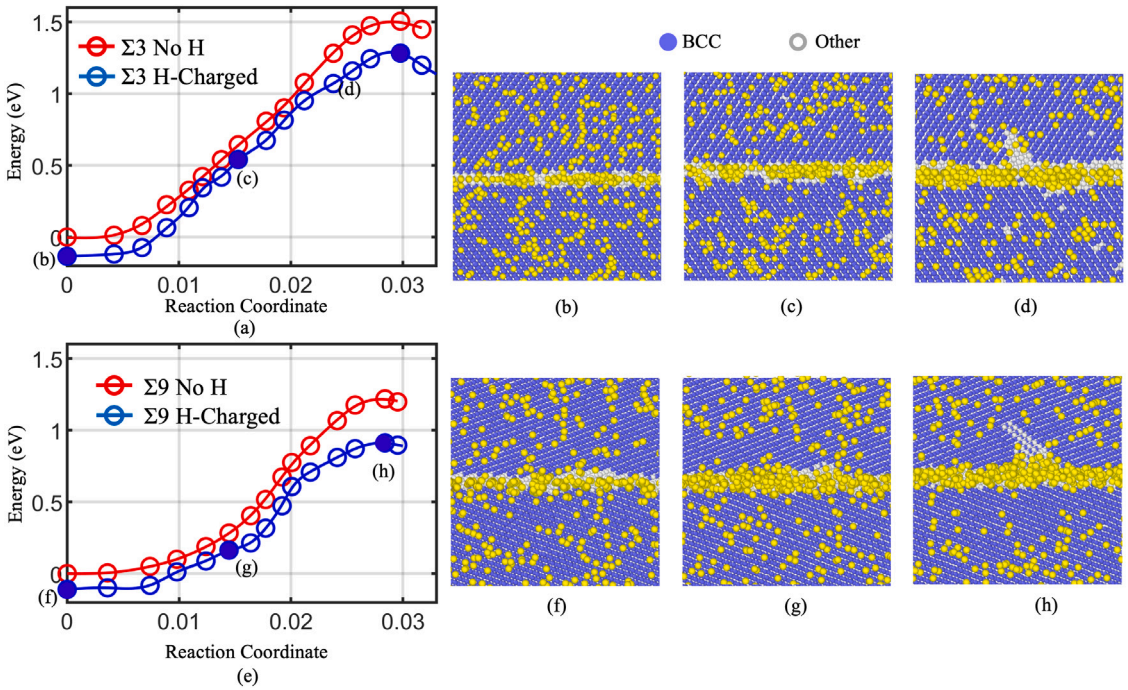

Fig. 12. NEB results for the defects generations at $\Sigma 3$ and $\Sigma 9$ GBs with and without hydrogen at a tensile displacement l_d = 5 Å. (a) MEPs of $\Sigma 3$ without hydrogen charged (red open circles) and with hydrogen charged (blue open circles). (b)–(d) Atomic configurations of replicas along the MEP for the GB with hydrogen charged. Their corresponding energies are plotted as solid blue circles in (a). (e) MEPs of $\Sigma 9$ without hydrogen charged (red open circles) and with hydrogen charged (blue open circles). (f)–(h) Atomic configurations of replicas along the MEP for the GB with hydrogen charged. Their corresponding energies are plotted as solid blue circles in (e). (For interpretation of the references to color in this figure legend, the reader is referred to the web version of this article.)

forming near the H clustering sites at the GB (Fig. 10a). By contrast, for $\Sigma 9$ GB, one curved dislocation with the Burger's vector of 1/2[111] is generated from the GB instead of the stacking faults. (b) the stacking faults near the $\Sigma 3$ GB continue to grow and form, and multiple curved dislocation lines (green) emit from both the GB and the stacking faults when $\varepsilon_{zz} = 0.046$. While the dislocation emitting from $\Sigma 9$ GB leaves no defect behind and migrates further into the grain as a straight line when $\varepsilon_{zz} = 0.041$. (c) Different from $\Sigma 3$ GB where multiple stacking faults forms when $\varepsilon_{zz} = 0.069$, dislocations keeps generating from $\Sigma 9$ GB and moves into the grain.

Upon a further increase of the tensile strain, the sample cannot sustain any more deformation by only emitting SFs or dislocations from the GB. At this stage, the local stress concentration may be released through GB cavitation and cracking. To confirm this, Fig. 11 presents the strain sequences of snapshots showing the defect structure evolution and then the subsequent failure process (cavity nucleation, growth, coalescence, and cracking) for $\Sigma 3$ and $\Sigma 9$ GBs, respectively. Several main findings from Fig. 11 are: (a) $\Sigma 3$ and $\Sigma 9$ GBs fail in different mechanisms. In detail, $\Sigma 3$ GB fractures through nano-void nucleation at several sites where PICH occurs, growth, and then coalescence (Fig. 11a). By contrast, $\Sigma 9$ GB fracture is seen to be dominated by one main cavity and then the crack growth along the GB (Fig. 11b). (b) At $\Sigma 3$ GB, the emission of partial dislocations on a plane neighboring to the previously activated slip plane has led to the formation of micro-twins (Fig. 11a). These micro-twins assist the growth of nano-voids. (c) At $\Sigma 9$ GB, accompanied by the GB cavitation and crack growth, only dislocation emission has been observed. Micro-twins are not seen near the $\Sigma 9$ GB.

3.3. H-dependent stress–strain curves, cohesive strength, and cohesive zone models

As a quantitative characterization of the effect of hydrogen on GB cohesive strength reduction, here we also perform Nudged Elastic Band (NEB) calculations to measure the energy barrier between the un-deformed and deformed configurations. In these calculations, the reaction coordinate is defined as the normalized path length along the minimum energy path (MEP) when the sample is deformed under a tensile strain, with the energy of the first replica along the MEP being set to zero.

Fig. 12 illustrates the results from NEB calculations. The converged MEPs for the $\Sigma 3$ GB without and with hydrogen are denoted by red and blue circles, respectively. At the same applied tensile displacement (l_d = 5Å), as shown in Fig. 12a, when hydrogen is present, the energy barrier for stacking fault nucleation from the $\Sigma 3$ GB decreases by 15%, from 1.51 eV to 1.28 eV. Figs. 12b-12d present the intermediate GB structures along the MEP. It shows the process of stacking fault nucleation and provides us with insights on how GB structure evolves in the presence and absence of H. In detail, Fig. 12b represents the first replica, which corresponds

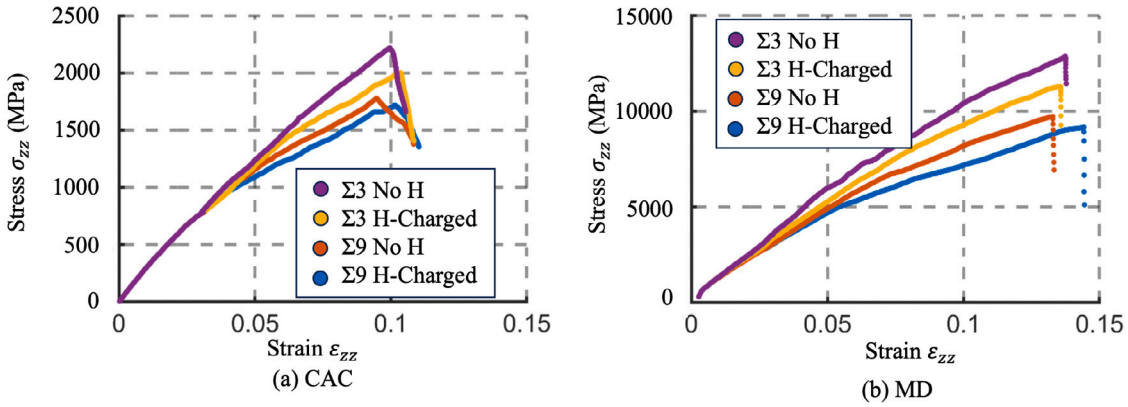

Fig. 13. Stress–strain curves for a bi-crystalline BCC iron sample containing a $\Sigma 3$ and $\Sigma 9$ GB under tension in the presence/absence of H from (a) CAC and (b) MD simulations, respectively. (For interpretation of the references to color in this figure legend, the reader is referred to the web version of this article.)

to the first local energy minimum on the MEP. At this stage, vacancies induced by the presence of hydrogen atoms lead to the relaxation of the GB structure. Upon a further increase of the applied tension, in conjunction with this relaxation, such GB structure changes eventually trigger the disorder of the GBs, as shown in Fig. 12c. At this stage, the stacking fault is observed to generate from $\Sigma 3$ GB.

By contrast, Figs. 12e presents the process of dislocation generation from $\Sigma 9$ GB. In Fig. 12e, the configuration represents a local energy minimum along the MEP path. Fig. 12h illustrates the final configuration for the dislocation generation from $\Sigma 9$ GB. Obviously, at this stage, the GB atoms have undergone a significant rearrangement. This final state represents a new energy minimum configuration where the GB has reached a steady-state structure that optimizes local stress distributions and minimizes potential energy. The MEP curves shown in Figs. 12a and 12e provide a quantitative description of the energy barrier responsible for the GB structure changes accompanied by the dislocation and stacking fault nucleation. Fig. 12a shows the MEP for $\Sigma 3$ GB without and with hydrogen. It shows that the presence of hydrogen significantly reduces the energy barrier for stacking fault nucleation, from 1.51 eV (red circles) to 1.28 eV (blue circles). Such an energy barrier reduction indicates that the presence of hydrogen atoms promotes dislocation nucleation. As further evidence, similar results have been observed in Fig. 12e, which shows the MEP for $\Sigma 9$ GB with and without hydrogen for comparison.

Fig. 13 presents the stress–strain curves resulting from CAC and MD simulations of a bi-crystalline BCC iron sample containing a $\Sigma 3$ and $\Sigma 9$ GB under tension in the presence and absence of H. The domain used in the CAC models for computing the stress–strain curve is a box with a dimension of 7 nm by 356 nm by 672 nm centered at the GB. A choice of this region assures that the calculated stress–strain curves have captured the material behavior resulting from the hydrogen diffusion dynamics, void nucleation, crack initiation/growth at the GB, and dislocation and stacking fault activities away from the GB. MD simulations are performed here in LAMMPS (Thompson et al., 2022) with the same boundary and loading conditions being applied on a nano-sized simulation cell with a dimension of 2 nm × 45 nm × 67 nm. For both CAC and MD simulations, the domain used for computing the stress state along z direction is the simulation box, as

$$P_{zz} = \frac{1}{V}\sum_{k=1}^{N} m_k v_{kz} v_{kz} + \frac{1}{V}\sum_{k=1}^{N'} r_{kz} f_{kz} \tag{3}$$

where N is the number of degrees of freedom (nodes and atoms for CAC simulations, and atoms for MD simulations), V is the simulation cell volume, m_k, v_{kz}, r_{kz}, and f_{kz} are the mass, velocity along z direction, position and force component along z direction. As the computation is in parallel for each subdomain, N' includes the subdomain atoms and elements, and $N' = N$ when the system is in serial and without periodic boundary conditions.

The CAC simulation-predicted stress–strain curves (Fig. 13a) for both $\Sigma 3$ and $\Sigma 9$ GBs under tension obey the classical elasticity initially, characterized by a linear relationship between stress and strain when the applied tensile strain is below 0.04. This indicates that the material's deformation is reversible and purely elastic up to 0.04 for a submicron-sized sample under consideration here. When the tensile strain is beyond 0.04, the samples' constitutive responses deviate from linear elasticity and start to deform plastically. At this stage, under the same tensile strain, the resulting stress in the model containing a $\Sigma 3$ GB is higher than that containing a $\Sigma 9$ GB. It implies that the $\Sigma 3$ GB has stronger resistance to plastic deformation. When the samples are charged with H, three main findings from the stress–strain curves in Fig. 13a are: (i) Both $\Sigma 3$ and $\Sigma 9$ GBs exhibit a notable reduction in the stress required to achieve the same level of strain, indicating that the presence of H severely reduces the material's resistance to deformation. (ii) the stress–strain curves for the H-charged specimen also exhibit a reduction in the elastic limit, implying the onset of an earlier plastic deformation than that in the sample containing no H. And (iii) the H-charged $\Sigma 9$ GB shows a significantly lower tensile strength than its non-H counterpart and even lower than H-charged $\Sigma 3$ GB, suggesting that the $\Sigma 9$ GB is more susceptible to HE. This finding highlights the importance of retaining the atomistic structures on the GB if one desires to predict the deformation behavior in polycrystalline alloys under H attack.

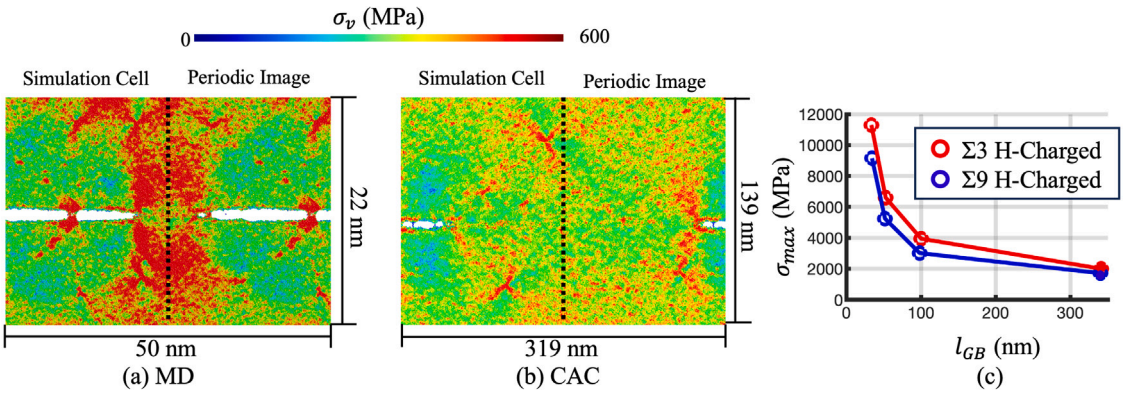

Fig. 14. The Von Mises stress field ahead of the tip of a GB crack in a bi-crystalline BCC iron sample containing a $\Sigma 9$ GB under tension in the presence of H from (a) nano-sized MD and (b) mesoscale CAC simulations. The dashed line shows the boundary between the simulation cell and its periodic image, and (c) yield stress for different grain sizes with open circles as MD simulations and solid circles for CAC simulations. (For interpretation of the references to color in this figure legend, the reader is referred to the web version of this article.)

For verification purposes, MD simulations of the failure of a nano-sized bi-crystalline BCC iron sample containing a $\Sigma 3$ and $\Sigma 9$ GB under tension in the presence/absence of H are also performed here. The stress–strain curves resulting from such MD simulations are shown in Fig. 13b. Several main observations from Fig. 13b are: (a) similar to CAC simulation results in Fig. 13a, the stress–strain curves are linear elastic when the applied tensile strain is 0.04 and below, and then followed by a non-linear plastic behavior. (b) no matter whether the sample is charged with H or not, the same level of tensile strain results in higher stress in $\Sigma 3$ GB than that in $\Sigma 9$ GB. (c) in the presence of H, the stress required to achieve the same level of strain in both GBs decreases, which gives rise to the reduction in the elastic limit and a decrease in cohesive strength, with the $\Sigma 9$ GB being more affected than the $\Sigma 3$ GB.

A comparison of Fig. 13a and Fig. 13b shows that, in both CAC and MD simulations, $\Sigma 3$ GB always exhibits higher cohesive strength than $\Sigma 9$ GB does, no matter it is charged with H or not. When the bi-crystalline BCC iron sample is charged with H, both CAC and MD simulations predict a GB cohesive strength reduction compared to the sample containing no H. The GB cohesive strengths predicted by MD are unreasonably high (≈10,000 MPa and above) and can be largely reduced (≈2000 MPa and below) if a submicron-sized CAC model is deployed. The unrealistic GB cohesive strength at a level of 10,000 MPa in MD is believed to originate from its limited simulation cell size. In detail, in MD models, the sample dimension along the GB crack growth direction is only tens of nanometers, which is insufficient to accommodate the long-range stress field ahead of the crack tip. As shown in Fig. 14a, the nano-sized MD simulation cell has cut off the long-range stress field ahead of the GB crack. As a consequence, the peak stress at which a GB crack starts to grow has been largely polluted by the stresses from its periodic images (see the dashed line in Fig. 14 for the boundary between the simulation cell and its periodic image). By contrast, when the sample size is scaled up to several hundred nanometers in CAC, the long-range internal stresses ahead of the GB crack tip can be well retained (Fig. 14b). Such an image stress-induced pollution can be largely reduced, and the prediction becomes more realistic. This observation highlights the importance of using a mesoscale model to accommodate the long-range internal stresses for predicting HE-induced material failure. Two additional MD simulations with the sample dimensions in them being increased towards that in CAC models are performed. The relevant simulation results are shown in Fig. 14c. It is seen that MD simulation results indeed converge towards CAC simulation results upon the increase of the sample dimension.

Different from MD and CAC, the cohesive zone model (CZM) remains one of the most widely used approaches for engineering-scale simulations of hydrogen embrittlement (Jemblie et al., 2017; Lin et al., 2022). However, CZMs often derive their force-separation laws from first-principles or atomistic simulations, which are limited in length scales and cut off the long-range stresses. Consequently, the CZMs extracted from such nanoscale simulations may lead to an overestimated GB cohesive strength (Fig. 13 and Fig. 14). Here, we argue the CAC-based CZM calibrations bring us a step closer to bridging these scales, offering improved accuracy compared to purely atomistic approaches. The incorporation of long-range stresses in CAC makes our model more comparable to experimental results.

Thus, as a preliminary attempt of further scaling up in length, here we also fit the mesoscale CAC simulation-predicted stress–strain curves into the cohesive zone model (CZM) (Xu and Needleman, 1993; Fernández-Sousa et al., 2022). Such CZM may find applications to describe the Mode-I cracking at a GB and its dependence on local H concentration. In this particular CZM, the traction–separation relation in the linear elastic region is expressed as:

$$\sigma = \frac{K}{\delta_0}\delta, \text{for } 0 \le \delta \le \delta_0 \tag{4}$$

The traction–separation relation in the softening region is expressed as:

$$\sigma = \sigma_{max}\left(1 - \frac{\delta - \delta_0}{\delta_f - \delta_0}\right), \text{for } \delta_0 \le \delta \le \delta_f \tag{5}$$

where σ is the cohesive stress and δ is the separation displacement.

Table 1
CAC simulation-based CZM parameters for Mode-I cracking at H-charged GBs.

Coefficients	σ_{max} (MPa)	δ_0 (nm)	δ_f (nm)
Σ3 (With H)	2003	69.602	72.928
Σ9 (With H)	1714	68.402	74.136
Σ3 (Without H)	2218	66.988	70.846
Σ9 (Without H)	1775	63.756	72.832

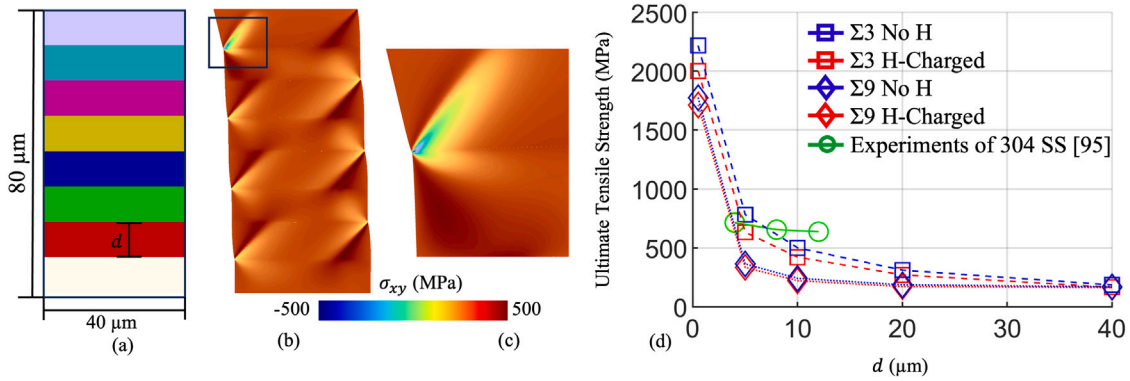

Fig. 15. (a) CZM model setup, (b) Shear stress contour for d = 10 μm, (c) a zoom-in view of the crack tip at the GB, (d) results comparing with experiments (Fan et al., 2019). (For interpretation of the references to color in this figure legend, the reader is referred to the web version of this article.)

The stress–strain curve in Fig. 13a is then fitted into the above CZM by considering: (i) the maximum traction σ_{max} as the peak value in the CAC simulation-predicted stress–strain curve. (ii) the δ_0 as the displacement at which the maximum traction σ_{max} is reached. And (iii) δ_f as the final separation displacement at which the bi-crystalline models completely separate. The resulting CZM parameters are listed in Table 1. Obviously, the CZM parameters are sensitive to both GB types/structures and H concentration. Incorporating such a GB structure and H concentration dependence through mesoscale simulations into the CZM is necessary if one desires to further improve the predictive capability of traditional CZM-based FE (Shishvan et al., 2023) or CPFE simulations.

As a preliminary attempt, we calibrated CAC-based cohesive zone models (CZM) for Σ3 and Σ9 grain boundaries (GBs), both with and without hydrogen, and implemented them into the MOOSE framework (Giudicelli et al., 2024). To simulate the intergranular fracture behavior in hydrogen-charged BCC iron with multiple GBs, we constructed CZM models containing multiple grains (with each grain oriented as shown in Fig. 2) and modeled them under plane strain conditions with dimensions of 40 μm × 80 μm, varying the layer thickness d from 5 μm to 40 μm. For each grain, the elastic constants were assigned based on MD results (Clavier et al., 2017) with hydrogen concentrations of 0.074 mol/L, and these were adjusted to match the specific orientations of Σ3 and Σ9 GBs, as shown in Fig. 15a. The bottom boundary was fixed, and displacement-controlled loading was applied at a strain rate of 10^{-6} /s, consistent with experimental conditions (Fan et al., 2019). To describe the constitutive behavior of the GBs, the CZM parameters for hydrogen-charged and non-hydrogen conditions were taken from Table 1.

According to the CAC-based CZM simulations, when the designed models reach their yield strength, a stress concentration develops at the crack tip of the cohesive elements, as illustrated in Fig. 15b and zoomed in Fig. 15c. Fig. 15d presents the ultimate tensile strength (UTS) as a function of layer thickness d for different GB configurations with hydrogen. For comparison, experimental data for 304 stainless steel (SS) (Fan et al., 2019), with grain sizes ranging from 4 μm to 12 μm, are included.

Key observations from the figure include: (a) For both Σ3 and Σ9 GBs, whether hydrogen is present or not, UTS decreases as the grain size d increases. This suggests that larger grains are more susceptible to failure, while smaller grains can withstand higher stresses. (b) Σ3 GBs, both with and without hydrogen, show slightly higher UTS than Σ9 GBs, which is consistent with established knowledge that Σ3 GBs generally exhibit greater resistance to fracture compared to Σ9 GBs. (c) The experimental results for 304 steel (Fan et al., 2019), shown as green circles (in Fig. 15d), demonstrate lower UTS values compared to our simulations. This is expected, as our simulations were conducted under idealized conditions with perfectly defined GBs, whereas real-world experimental samples contain imperfections and microstructural defects that reduce the overall strength.

It is important to acknowledge that pure BCC iron, while useful for understanding fundamental mechanisms of plasticity and defect nucleation, is not a practical structural material. Practical steels, like 304 steel (Fan et al., 2019), consist of multiple alloying elements and phases, and the GBs in these materials are more complex. However, many steels share a BCC crystal structure with pure iron, allowing us to extrapolate some of our findings to practical systems. Our CZM model is based on a columnar grain structure of pure BCC iron, while the experimental results are from 304 steel, which has random grain boundaries with various misorientation angles. This difference in material system and microstructure may explain the discrepancies between the simulated and experimental UTS values.

4. Summary

To summarize, this paper presents an atomistic-to-mesoscale computational analysis of the failure behavior in an H-charged bi-crystalline BCC iron sample under deformation through CAC simulations. Taking the bi-crystalline BCC iron sample containing the H-charged $\Sigma 3$ and $\Sigma 9$ GBs under tension as a test bed, our main findings from this research are: (1) the failure of H-charged GBs during the HE of polycrystalline alloys occurs through the cooperation of diffusion, plastic flow, void nucleation, coalescence, crack initiation, and growth across a wide range of length scales. A prediction of it is beyond the reach of existing single-scale or scale-separation approaches. It necessitates concurrent multi-scale simulations. (2) the plastic deformation promotes H atom diffusion and its clustering at the GB. Such a PICH mechanism is considered an intermediate process before HEDE but after HELP. It plays an important role in the subsequent GB cavitation and cracking. This finding highlights the possibility of a HELP-PICH-HEDE process responsible for HE-induced GB fracture. We believe PICH is crucial for bridging the macroscopic HELP mechanism and the atomistic HEDE mechanism. Neither HELP nor HEDE alone sufficiently captures the complexity of HE. Instead, the interply between HELP and HEDE is facilitated by PICH. A cooperation of these three mechanisms is necessary for HE-induced crack initiation and growth. (3) the H diffusion exhibits a strong dependence on GB structures. It diffuses faster on the GB, such as $\Sigma 9$ GB, with a larger free volume than it does on the GB, such as $\Sigma 3$ GB, with a smaller free volume. As a consequence, multiple PICH sites simultaneously appear at $\Sigma 3$ GB, but only one PICH site dominates at $\Sigma 9$ GB. (4) the GB failure mechanism also strongly depends on GB structures. In detail, $\Sigma 3$ GB fails through micro-twinning, multiple void nucleation, growth, and coalescence, while $\Sigma 9$ GB fractures through dislocation emission, crack initiation, and growth. (5) The presence of H atoms at the GB significantly decreases the cohesive strengths of GBs. No matter whether the sample is charged with H or not, $\Sigma 3$ GB always exhibits higher cohesive strength than $\Sigma 9$ GB does, and (6) the nanoscale MD simulation overestimates the GB cohesive strength due to its limited simulation cell. By contrast, with the capability of accommodating the long-range internal stresses and far-field dislocation activities, CAC simulations predict a reasonably lower GB cohesive strength. A calibration of the CZMs from CAC simulations may largely improve the predictive capability of the higher scale computer models, such as CPFE+CZM (Wu and Zikry, 2015; Pu et al., 2017; Pouillier et al., 2012; Singh et al., 2022; Liu et al., 2021), for understanding the H-induced cracking in plastically deformed polycrystalline alloys at engineering scales.

5. Discussion

Despite their potential to support the understanding of HE, the above findings need to be taken with caution due to the limitations in the following several aspects:

(1) the CAC model with a dimension of hundreds of nanometers indeed gets one step closer to that in experiments. It is, however, still insufficient to accommodate the long-range internal stress induced by the accumulation of a large population of dislocations at the GB, which was found to span a range of tens of microns in experiments (Guo et al., 2015). There thus exists a need to further scale up in lengths by developing computationally more efficient CAC solvers, such as GPU-based CAC, that can leverage the newest development in computing power.

(2) One of the discrepancies observed in our simulations is that the predicted failure stresses read significantly higher than those measured in experiments. We attribute this difference to several factors: (a) the smaller sample sizes in our simulations. The sample size in our CAC simulations is larger than MD samples but is still smaller than that in experiments. (b) the perfect GB structures in our models. The GBs under consideration here contain no defects, such as vacancies or precipitates, which are commonly observed in experimental samples. And (c) the empirical interatomic potential used in this work may lead to an overestimated GB cohesive strength.

(3) the H-induced material failure process does not only span a wide range of length scales but also occurs across multiple time scales. It remains a challenge using any single time-scale approach to simultaneously model the fast motion of a dislocation line together with the slow H hopping along the line. The implementation of a multiple timescale algorithm into the present CAC is necessary to address this challenge, for instance, integration of CAC with the Nudged Elastic Band (NEB) and kinetic Monte Carlo (kMC). NEB will allow for the calculation of energy barriers for void nucleation and crack initiation, which can then be informed into kMC to extend the simulation timescales to effectively capture the rare, low-energy events that occur over longer periods. This is essential for simulating HE over an experimentally comparable duration.

(4) HE not only couples deformation with diffusion but also couples with thermal transport. The effects of temperatures on the HE process in an open environment often cannot be simply ignored. In this scenario, an expansion of our recent finite-temperature algorithm (Ji et al., 2022, 2024) into CAC towards a thermo-mechanical coupling simulation is needed.

(5) the GB in polycrystalline materials does not exist in isolation. It is always embedded within a complex environment. The cohesive strength of an H-charged GB in a bi-crystalline sample may differ from that in bulk because the effects of the surrounding microstructure on the fracture behavior along the GB have been ignored in a bi-crystalline set-up. A characterization of the microstructure dependence of the GB fracture through CAC simulation of the failure of polycrystalline materials, in turn, becomes necessary.

(6) similar to MD, the predictive capability of CAC is largely determined by the reliability of the interatomic potential. As the demonstration of a concept, the EAM potential (Song and Curtin, 2012) for Fe-Fe and Fe-H interaction has been deployed here. Compared with density functional theory (DFT) calculations, the deployment of such empirical potentials does significantly gain in computation efficiency but may not be able to address the full complexity of H-induced bond weakening. Fortunately, the machine learned interatomic potential (Meng et al., 2021) that is more efficient than DFT but retains a DFT-comparable accuracy was recently developed. Such a high-fidelity interatomic force field is important for considering the formation of molecular hydrogen at high

concentrations, which could influence void and crack initiation in HE. This, however, has been ignored in the EAM force field (Song and Curtin, 2012) deployed here, which gives rise to a high repulsive force when two hydrogen ions get very close to each other. We believe a simulation of the hydrogen molecule formations requires the deployment of a reactive force field to enable bond formation and breaking, which often demands significantly higher computational costs than EAM does. The CAC simulation tool to be furnished with such interatomic force fields is under development. Our future work will explore its applicability in simulating the hydrogen molecule formation in the process of HE. A further improvement of the predictive capability of CAC is equipping it with reactive or DFT-informed machine learning potential.

CRediT authorship contribution statement

Yipeng Peng: Writing – review & editing, Writing – original draft, Visualization, Software, Methodology, Investigation, Formal analysis, Data curation, Conceptualization. **Thanh Phan:** Writing – review & editing, Software. **Haibo Zhai:** Writing – review & editing, Supervision, Resources, Project administration, Funding acquisition, Conceptualization. **Liming Xiong:** Writing – review & editing, Supervision, Methodology, Conceptualization. **Xiang Zhang:** Writing – review & editing, Supervision, Resources, Project administration, Methodology, Conceptualization.

Declaration of competing interest

The authors declare that they have no known competing financial interests or personal relationships that could have appeared to influence the work reported in this paper.

Acknowledgment

This work has been funded by the Wyoming Innovation Partnership Program through the project *Advancing Blue Hydrogen Production and Transport Infrastructure in Wyoming*. The high-performance computing resources and support from the NCAR-Wyoming Supercomputing Center (NWSC) and the Advanced Research Computing Center (ARCC) at the University of Wyoming are also greatly acknowledged. LX acknowledges the support of the U.S. National Science Foundation (CMMI-2322675 and CMMI-2328533) and the Advanced Cyberinfrastructure Coordination Ecosystem: Services & Support (XSEDE-TG-MSS170003 and XSEDE-TG-MSS190008).

Data availability

Data will be made available on request.

References

Abdolvand, H., 2019. Progressive modelling and experimentation of hydrogen diffusion and precipitation in anisotropic polycrystals. Int. J. Plast. 116, 39–61.
An, D., Krieger, W., Zaefferer, S., 2020. Unravelling the effect of hydrogen on microstructure evolution under low-cycle fatigue in a high-manganese austenitic TWIP steel. Int. J. Plast. 126, 102625.
Arnaudov, N., Kolyshkin, A., Weihe, S., 2020. Micromechanical modeling of fatigue crack initiation in hydrogen atmosphere. Mech. Mater. 149, 103557.
Asano, S., Otsuka, R., 1976. The lattice hardening due to dissolved hydrogen in iron and steel. Scr. Mater. 10, 1015–1020.
Barrera, O., Tarleton, E., Tang, H., Cocks, A., 2016. Modelling the coupling between hydrogen diffusion and the mechanical behaviour of metals. Comput. Mater. Sci. 122, 219–228.
Barrows, W., Dingreville, R., Spearot, D., 2016. Traction–separation relationships for hydrogen induced grain boundary embrittlement in nickel via molecular dynamics simulations. Mater. Sci. Eng. A 650, 354–364.
Beachem, C., 1972. A new model for hydrogen-assisted cracking (hydrogen embrittlement). Metall. Mater. Trans. B 3, 437–451.
Bearman, R.J., Kirkwood, J.G., 1958. Statistical mechanics of transport processes. XI. Equations of transport in multicomponent systems. J. Chem. Phys. 28 (1), 136–145.
Birnbaum, H., Sofronis, P., 1994. Hydrogen-enhanced localized plasticity - a mechanism for hydrogen related fracture. Mater. Sci. Eng. A 176, 191–202.
Charles, Y., Nguyen, H., Gasperini, M., 2017. Comparison of hydrogen transport through pre-deformed synthetic polycrystals and homogeneous samples by finite element analysis. Int. J. Hydrog. Energy 42, 20336–20350.
Chen, Y., 2006. Local stress and heat flux in atomistic systems involving three-body forces. J. Chem. Phys. 124, 054113.
Chen, Y., 2009. Reformulation of microscopic balance equations for multiscale materials modeling. J. Chem. Phys. 130, 134706.
Chen, Y., 2016. The origin of the distinction between microscopic formulas for stress and Cauchy stress. Europhys. Lett. 116, 34003.
Chen, Y., 2024. Asymmetry of the atomic-level stress tensor in homogeneous and inhomogeneous materials. Proc. R. Soc. A 480, 20230606.
Chen, Y., Diaz, A., 2016. Local momentum and heat fluxes in transient transport processes and inhomogeneous systems. Phys. Rev. E 98, 052113.
Chen, Y., Diaz, A., 2018. Physical foundation and consistent formulation of atomic-level fluxes in transport processes. Phys. Rev. E 98, 052113.
Chen, H., Xu, S., Li, W., Ji, R., Phan, T., Xiong, L., 2018. A spatial decomposition parallel algorithm for a concurrent atomistic-continuum simulator and its preliminary applications. Comput. Mater. Sci. 144, 1–10.
Chen, J., Zhu, Y., Huang, M., Zhao, L., Liang, S., Li, Z., 2021. Study on hydrogen-affected interaction between dislocation and grain boundary by MD simulation. Comput. Mater. Sci. 196, 110562.
Clavier, G., Desbiens, N., Bourasseau, E., Lachet, V., Brusselle-Dupend, N., Rousseau, B., 2017. Computation of elastic constants of solids using molecular simulation: comparison of constant volume and constant pressure ensemble methods. Mol. Simul. 43 (17), 1413–1422.
Deng, Y., Barnoush, A., 2018. Hydrogen embrittlement revealed via novel in situ fracture experiments using notched micro-cantilever specimens. Acta Mater. 142, 236–247.
Fan, Y., Zhang, B., Wang, J., Han, E.-H., Ke, W., 2019. Effect of grain refinement on the hydrogen embrittlement of 304 austenitic stainless steel. J. Mater. Sci. Technol. 35 (10), 2213–2219.

Fernández-Sousa, R., Betegón, C., Martínez-Paneda, E., 2022. Cohesive zone modelling of hydrogen assisted fatigue crack growth: The role of trapping. Int. J. Fatigue 162, 106935.
Ferreira, P., Robertson, I., Birnbaum, H., 1998. Hydrogen effects on the interaction between dislocations. Acta Mater. 46 (5), 1749–1757.
Fujihara, H., Toda, H., Ebihara, K.-i., Kobayashi, M., Mayama, T., Hirayama, K., Shimizu, K., Takeuchi, A., Uesugi, M., 2024. Assessment of hydrogen embrittlement behavior in Al-Zn-Mg alloy through multi-modal 3D image-based simulation. Int. J. Plast. 174, 103897.
Giudicelli, G., Lindsay, A., Harbour, L., Icenhour, C., Li, M., Hansel, J.E., German, P., Behne, P., Marin, O., Stogner, R.H., Miller, J.M., Schwen, D., Wang, Y., Munday, L., Schunert, S., Spencer, B.W., Yushu, D., Recuero, A., Prince, Z.M., Nezdyur, M., Hu, T., Miao, Y., Jung, Y.S., Matthews, C., Novak, A., Langley, B., Truster, T., Nobre, N., Alger, B., Andrš, D., Kong, F., Carlsen, R., Slaughter, A.E., Peterson, J.W., Gaston, D., Permann, C., 2024. 3.0 - MOOSE: Enabling massively parallel multiphysics simulations. SoftwareX 26, 101690, URL: https://www.sciencedirect.com/science/article/pii/S235271102400061X.
Gong, P., Turk, A., Nutter, J., Yu, F., Wynne, B., Rivera-Diaz-del Castillo, P., Rainforth, W.M., 2022. Hydrogen embrittlement mechanisms in advanced high strength steel. Acta Mater. 223, 117488.
Guo, Y., Collins, D., Tarleton, E., Hofmann, F., Tischler, J., Liu, W., Xu, R., Wilkinson, A., Britton, T., 2015. Measurement of stress fields near a grain boundary exploring blocked arrays of dislocations in 3D. Acta Mater. 96, 229–236.
Hassan, U., Govind, K., Hartmaier, A., 2019. Micromechanical modelling of coupled crystal plasticity and hydrogen diffusion. Phil. Mag. 99, 92–115.
Huang, L., Chen, D., Xie, D., Li, S., Zhang, Y., Zhu, T., Raabe, D., Ma, E., Li, J., Shan, Z., 2023. Quantitative tests revealing hydrogen-enhanced dislocation motion in α-iron. Nature Mater. 22, 710–716.
Hussein, A., Krom, A., Dey, P., Sunnardianto, G., Moultos, O., Walters, C., 2021. The effect of hydrogen content and yield strength on the distribution of hydrogen in steel: a diffusion coupled micromechanical FEM study. Acta Mater. 209, 116799.
Ilin, D., Saintier, N., Olive, J., Abgrall, R., Aubert, I., 2014. Simulation of hydrogen diffusion affected by stress-strain heterogeneity in polycrystalline stainless steel. Int. J. Hydrog. Energy 39, 2418–2422.
Irving, J., Kirkwood, J.G., 1950. The statistical mechanical theory of transport processes. IV. The equations of hydrodynamics. J. Chem. Phys. 18 (6), 817–829.
Isfandbod, M., Martínez-Pañeda, E., 2021. A mechanism-based multi-trap phase field model for hydrogen assisted fracture. Int. J. Plast. 144, 103044.
Jemblie, L., Olden, V., Akselsen, O.M., 2017. A coupled diffusion and cohesive zone modelling approach for numerically assessing hydrogen embrittlement of steel structures. Int. J. Hydrog. Energy 42 (16), 11980–11995.
Ji, R., Adrian, D., Li, W., Xiong, L., Chen, Y., 2018. Asymmetry of the atomic-level stress tensor in homogeneous and inhomogeneous materials. Proc. R. Soc. A 474, 20180155.
Ji, R., Phan, T., Chen, Y., McDowell, D., Xiong, L., 2022. A finite-temperature coarse-grained atomistic approach for understanding the kink-controlled dynamics of micrometer-long dislocations in high-Peierls-barrier materials. MRS Commun. 1–9.
Ji, R., Phan, T., Chen, Y., McDowell, D., Xiong, L., 2024. An atomistic-to-microscale characterization of the kink-controlled dislocation dynamics in bcc metals through finite-temperature coarse-grained atomistic simulations. Acta Mater. 262, 119440.
Johnson, W., 1875. On some remarkable changes produced in iron and steel by the action of hydrogen and acids. Nature 11, 393.
Kacher, J., Robertson, I., 2012. Quasi-four-dimensional analysis of dislocation interactions with grain boundaries in 304 stainless steel. Acta Mater. 60 (19), 6657–6672.
Khanchandani, H., Rolli, R., Schneider, H.-C., Kirchlechner, C., Gault, B., 2023. Hydrogen embrittlement of twinning-induced plasticity steels: Contribution of segregation to twin boundaries. Scr. Mater. 225, 115187.
Kim, J., Tasan, C., 2019. Microstructural and micro-mechanical characterization during hydrogen charging: An in situ scanning electron microscopy study. Int. J. Hydrog. Energy 12, 6333–6343.
Kimizuka, H., Ogata, S., 2011. Slow diffusion of hydrogen at a screw dislocation core in α-iron. Phys. Rev. B 84 (2), 024116.
Kirkwood, J.G., 1946. The statistical mechanical theory of transport processes I. General theory. J. Chem. Phys. 14 (3), 180–201.
Kirkwood, J.G., 1947. The statistical mechanical theory of transport processes II. Transport in gases. J. Chem. Phys. 15 (1), 72–76.
Koyama, M., Taheri-Mousavi, S., Yan, H., Kim, J., Cameron, B., Moeini-Ardakani, S., Li, J., Tasan, C., 2020. Origin of micrometer-scale dislocation motion duringhydrogen desorption. Sci. Adv. 6, 1–8.
Koyama, M., Tasan, C., Akiyama, E., Tsuzaki, K., Raabe, D., 2014. Hydrogen-assisted decohesion and localized plasticity in dual-phase steel. Acta Mater. 70, 174–187.
Li, Y., Li, W., Hu, J.C., Song, H.M., Jin, X.J., 2017. Compatible strain evolution in two phases due to epsilon martensite transformation in duplex TRIP-assisted stainless steels with high hydrogen embrittlement resistance. Int. J. Plast. 88, 53–69.
Li, Y., Li, W., Min, N., Liu, H., Jin, X., 2020. Homogeneous elasto-plastic deformation and improved strain compatibility between austenite and ferrite in a co-precipitation hardened medium Mn steel with enhanced hydrogen embrittlement resistance. Int. J. Plast. 133, 102805.
Li, K., Tang, B., Zhang, M., Zhao, L., Liu, X., Fan, J., Li, J., 2023. A hydrogen diffusion model considering grain boundary characters based on crystal plasticity framework. Int. J. Plast. 169, 103740.
Liang, S., Huang, M., Zhao, L., Zhu, Y., Li, Z., 2021. Effect of multiple hydrogen embrittlement mechanisms on crack propagation behavior of FCC metals: Competition vs. synergy. Int. J. Plast. 143, 103023.
Lin, M., Yu, H., Wang, X., Wang, R., Ding, Y., Alvaro, A., Olden, V., He, J., Zhang, Z., 2022. A microstructure informed and mixed-mode cohesive zone approach to simulating hydrogen embrittlement. Int. J. Hydrog. Energy 47 (39), 17479–17493.
Liu, Y., El Chamaa, S., Wenman, M.R., Davies, C.M., Dunne, F.P., 2021. Hydrogen concentration and hydrides in Zircaloy-4 during cyclic thermomechanical loading. Acta Mater. 221, 117368.
Lynch, S., 2011. Interpreting hydrogen-induced fracture surfaces in terms of deformation processes: A new approach. Scr. Mater. 65, 851–854.
Martin, M.L., Connolly, M.J., DelRio, F.W., Slifka, A.J., 2020. Hydrogen embrittlement in ferritic steels. Appl. Phys. Rev. 7 (4).
Martin, M.L., Dadfarnia, M., Nagao, A., Wang, S., Sofronis, P., 2019. Enumeration of the hydrogen-enhanced localized plasticity mechanism for hydrogen embrittlement in structural materials. Acta Mater. 165, 734–750.
Matsui, H., Kimura, H., Moriya, S., 1979. The effect of hydrogen on the mechanical properties of high purity iron I. Softening and hardening of high purity iron by hydrogen charging during tensile deformation. Mater. Sci. Eng. 40, 207–216.
Meng, F., Du, J.P., Shinzato, S., Mori, H., Yu, P., Matsubara, K., Ishikawa, N., Ogata, S., 2021. General-purpose neural network interatomic potential for the α-iron and hydrogen binary system: Toward atomic-scale understanding of hydrogen embrittlement. Phys. Rev. Mater. 5, 113606.
Novak, P., Yuan, R., Somerday, B., Sofronis, P., Ritchie, R., 2010. A statistical, physical-based, micro-mechanical model of hydrogen-induced intergranular fracture in steel. J. Mech. Phys. Solids 58, 206–226.
Okuno, K., Takai, K., 2023. Determination of hydrogen diffusibility and embrittlement susceptibility of high-strength steel evaluated at different temperatures based on the local equilibrium theory. Acta Mater. 246, 118725.
Peng, Y., Ji, R., Phan, T., Capolungo, L., Levitas, V., Xiong, L., 2023a. Effect of a micro-scale dislocation pileup on the atomic-scale multi-variant phase transformation and twinning. Comput. Mater. Sci. 230, 112508.
Peng, Y., Ji, R., Phan, T., Chen, X., Zhang, N., Xu, S., Bastawros, A., Xiong, L., 2023b. Effect of a long-range dislocation pileup on the atomic-scale hydrogen diffusion near a grain boundary in plastically deformed bcc iron. Crystals 13, 1270.
Peng, Y., Ji, R., Phan, T., Gao, W., Levitas, V., Xiong, L., 2022. An atomistic-to-microscale computational analysis of the dislocation pileup-induced local stresses near an interface in plastically deformed two-phase materials. Acta Mater. 226, 117663.

Pfeil, L.B., 1926. The effect of occluded hydrogen on the tensile strength of iron. Proc. R. Soc. A 112 (760), 182–195.
Pouillier, E., Gourgues, A.-F., Tanguy, D., Busso, E.P., 2012. A study of intergranular fracture in an aluminium alloy due to hydrogen embrittlement. Int. J. Plast. 34, 139–153.
Pu, C., Gao, Y., Wang, Y., Sham, T., 2017. Diffusion-coupled cohesive interface simulations of stress corrosion intergranular cracking in polycrystalline materials. Acta Mater. 136, 21–31.
Rimoli, J., Ortiz, M., 2010. A three-dimensional multiscale model of intergranular hydrogen-assisted cracking. Phil. Mag. 90, 2939–2963.
Robertson, I., 2001. The effect of hydrogen on dislocation dynamics. Eng. Fract. Mech. 68, 671–692.
Robertson, I.M., Sofronis, P., Nagao, A., Martin, M., Wang, S., Gross, D., Nygren, K., 2015. Hydrogen embrittlement understood. Metall. Mater. Trans. A 46 (6), 2323–2341.
Saintier, N., Awane, T., Olive, J.-M., Matsuoka, S., Murakami, Y., 2011. Analyses of hydrogen distribution around fatigue crack on type 304 stainless steel using secondary ion mass spectrometry. Int. J. Hydrog. Energy 36 (14), 8630–8640.
Sanchez, J., Fullea, J., Andrade, M., De Andres, P., 2010. Ab initio molecular dynamics simulation of hydrogen diffusion in α-iron. Phys. Rev. B 81 (13), 132102.
Shishvan, S., Csányi, G., Deshpande, V., 2023. Strain rate sensitivity of the hydrogen embrittlement of ferritic steels. Acta Mater. 257, 119173.
Singh, V., Kumar, R., Charles, Y., Mahajan, D.K., 2022. Coupled diffusion-mechanics framework for simulating hydrogen assisted deformation and failure behavior of metals. Int. J. Plast. 157, 103392.
Sofronis, P., McMeeking, R., 1989. Numerical analysis of hydrogen transport near a blunting crack tip. J. Mech. Phys. Solids 37, 317–350.
Song, J., Curtin, W., 2011. A nanoscale mechanism of hydrogen embrittlement in metals. Acta Mater. 59, 1557–1569.
Song, J., Curtin, W., 2012. Atomic mechanism and prediction of hydrogen embrittlement in iron. Nature Mater. 12, 145–151.
Song, J., Curtin, W., 2014. Mechanisms of hydrogen-enhanced localized plasticity: An atomistic study using a-fe as a model system. Acta Mater. 68, 61–69.
Strauch, B., Pilz, P., Hierold, J., Zimmer, M., 2023. Experimental simulations of hydrogen migration through potential storage rocks. Int. J. Hydrog. Energy 48 (66), 25808–25820.
Stukowski, A., 2009. Visualization and analysis of atomistic simulation data with OVITO–the open visualization tool. Modelling Simul. Mater. Sci. Eng. 18 (1), 015012.
Stukowski, A., Bulatov, V.V., Arsenlis, A., 2012. Automated identification and indexing of dislocations in crystal interfaces. Modelling Simul. Mater. Sci. Eng. 20 (8), 085007.
Su, Y., Phan, T., Xiong, L., Kacher, J., 2023. Multiscale computational and experimental analysis of slip-GB reactions: in situ high-resolution electron backscattered diffraction and concurrent atomistic-continuum simulations. Scr. Mater. 232, 115500.
Thompson, A.P., Aktulga, H.M., Berger, R., Bolintineanu, D.S., Brown, W.M., Crozier, P.S., in 't Veld, P.J., Kohlmeyer, A., Moore, S.G., Nguyen, T.D., Shan, R., Stevens, M.J., Tranchida, J., Trott, C., Plimpton, S.J., 2022. LAMMPS - a flexible simulation tool for particle-based materials modeling at the atomic, meso, and continuum scales. Comput. Phys. Comm. 271, 108171.
Tondro, A., Taherijam, M., Abdolvand, H., 2023. Diffusion and redistribution of hydrogen atoms in the vicinity of localized deformation zones. Mech. Mater. 177, 104544.
Wan, L., Geng, W., Ishii, A., Du, J., Mei, Q., Ishikawa, N., Kimizuka, H., Ogata, S., 2019. Hydrogen embrittlement controlled by reaction of dislocation with grain boundary in alpha-iron. Int. J. Plast. 112, 206–219.
Warner, D., Curtin, W., Qu, S., 2007. Rate dependence of crack-tip processes predicts twinning trends in f.c.c. metals. Nature Mater. 6, 876–881.
Wigner, E., Seitz, F., 1933. On the constitution of metallic sodium. Phys. Rev. 43, 804.
Wu, Q., Zikry, M., 2015. Prediction of diffusion assisted hydrogen embrittlement failure in high strength martensitic steels. J. Mech. Phys. Solids 85, 143–159.
Xiong, L., Chen, Y., 2009a. Coarse-grained simulations of single-crystal silicon. Modelling Simul. Mater. Sci. Eng. 17, 035002.
Xiong, L., Chen, Y., 2009b. Multiscale modeling and simulation of single-crystal MgO through an atomistic field theory. Int. J. Solids Struct. 46, 1448–1455.
Xiong, L., Deng, Q., Tucker, G., McDowell, D., Chen, Y., 2012a. Coarse-grained atomistic simulations of dislocations in Al, Ni and Cu crystals. Int. J. Plast. 38, 86–101.
Xiong, L., Deng, Q., Tucker, G., McDowell, D., Chen, Y., 2012b. A concurrent scheme for passing dislocations from atomistic to continuum domains. Acta Mater. 60, 899–913.
Xiong, L., McDowell, D.L., Chen, Y., 2012c. Nucleation and growth of dislocation loops in Cu, Al and Si by a concurrent atomistic-continuum method. Scr. Mater. 67 (7–8), 633–636, Publisher: Elsevier.
Xiong, L., Tucker, G., McDowell, D., Chen, Y., 2011. Coarse-grained atomistic simulation of dislocations. J. Mech. Phys. Solids 59, 160–177.
Xu, X.-P., Needleman, A., 1993. Void nucleation by inclusion debonding in a crystal matrix. Modelling Simul. Mater. Sci. Eng. 1 (2), 111.
Xu, S., Payne, T., Chen, H., Liu, Y., Xiong, L., Chen, Y., McDowell, D., 2018. PyCAC: The concurrent atomistic-continuum simulation environment. J. Mater. Res. 33, 857–871.
Xu, S., Xiong, L., Chen, Y., McDowell, D., 2017. Validation of the concurrent atomistic-continuum method on screw dislocation/stacking fault interactions. Crystals 7, 120.
Yang, S., Chen, Y., 2015. Concurrent atomistic and continuum simulation of bi-crystal strontium titanate with tilt grain boundary. Proc. R. Soc. A 471, 20140758.
Yavas, D., Phan, T., Xiong, L., Hebert, K., Bastawros, A., 2020. Mechanical degradation due to vacancies produced by grain boundary corrosion of steel. Acta Mater. 200, 471–480.
Yin, S., Cheng, G., Chang, T.-H., Richter, G., Zhu, Y., Gao, H., 2019. Hydrogen embrittlement in metallic nanowires. Nature Commun. 10 (1), 2004.
Zhou, X., Marchand, D., McDowell, D.L., Zhu, T., Song, J., 2016a. Chemomechanical origin of hydrogen trapping at grain boundaries in fcc metals. Phys. Rev. Lett. 116 (7), 075502.
Zhou, X., Ouyang, B., Curtin, W., Song, J., 2016b. Atomistic investigation of the influence of hydrogen on dislocation nucleation during nanoindentation in Ni and Pd. Acta Mater. 116, 364–369.
Zhou, X.-Y., Zhu, J.-H., Wu, H.-H., 2021. Molecular dynamics studies of the grain-size dependent hydrogen diffusion coefficient of nanograined Fe. Int. J. Hydrog. Energy 46 (7), 5842–5851.
Zirkle, T., Costello, L., McDowell, D., 2021. Crystal plasticity modeling of hydrogen and hydrogen-related defects in initial yield and plastic flow of single-crystal stainless steel 316L. Metall. Mater. Trans. A 52A, 3961–3977.